Investigating the role of dust in ice nucleation within clouds and further effects on the regional weather system over East Asia

Part I: model development and validation

Lin Su[1], and Jimmy C.H. Fung[2, 3]

[1] School of Science, Hong Kong University of Science and Technology, Hong Kong, China

[2] Division of Environment, Hong Kong University of Science and Technology, Hong Kong, China

[3] Department of Mathematics, Hong Kong University of Science and Technology, Hong Kong, China

Correspondence to: Lin Su (lsu@connect.ust.hk)

Highlights:

A new treatment has been implemented in a regional model for evaluating the role of dust particles in atmospheric ice nucleation.

The effect of dust on atmospheric IWC over East Asia during a dust-intensive period is simulated.

The simulation of atmospheric IWC during dust events is substantially improved upon the effect of dust being considered.

1

Abstract. The GOCART–Thompson microphysics scheme coupling the GOCART aerosol model and the aerosol-aware Thompson-Eidhammer microphysics scheme has been implemented in WRF-Chem, to quantify and evaluate the effect of dust on the ice nucleation process in the atmosphere by serving as ice nuclei (IN). The performance of the GOCART-Thompson microphysics scheme in simulating the effect of dust in atmospheric ice nucleation is then evaluated over East Asia during spring, a typical dust-intensive season, in 2012. Based upon the dust emission reasonably reproduced by WRF-Chem, the effect of dust on atmospheric cloud ice water content (IWC) is well reproduced. With abundant dust particles serving as IN, the simulated ice water mixing ratio and ice crystal number concentration increases up to one order of magnitude over the dust source region and downwind areas during the investigated period. The comparison with ice water path from satellite observations demonstrated that the simulation of cloud ice profile is substantially improved by considering the indirect effect of dust particles in the simulations. Additional sensitivity experiments are carried out to optimize the parameters in the ice nucleation parameterization in the GOCART–Thompson microphysics scheme. Results suggest that lowering the threshold relative humidity 00% for the ice nucleation parameterization leads to further improvement in cloud ice simulation.

2

1 Introduction

Dust aerosol is the second largest contributor to the global aerosol burden (Textor et al., 2006), and it is estimated to contribute around 20% to the annual global aerosol emission (Tomasi et al., 2017). The Intergovernmental Panel on Climate Change (IPCC) has recognized dust as a major component of atmospheric aerosols, which are an "essential climate variable." East Asia is a main contributor to the Earth's dust emission. It has been reported in previous studies that East Asian dust contributes 25–50% of global emission, depending on the climate of the particular year (Ginoux et al., 2001).

Dust in the atmosphere alters the Earth's weather and climate through certain ways. By reflecting, absorbing and scattering the incoming solar radiation, dust can cause a warming effect within the atmosphere and a cooling effect at the surface layer (Lacis, 1995), which is the direct effect of dust. The semi-direct effect of dust is related to the absorption of short-wave and long-wave radiation by dust aerosol within clouds, leading to a warming of the surrounding environment, causing a shrinking of cloud and a lower cloud albedo, and thus modifying the radiation budget (Perlwitz and Miller, 2010;Hansen et al., 1997). The dust-cloud-interaction is also referred to as the indirect effect of dust. Dust particles are recognized as effective IN and play an important role in the ice nucleation process in the atmosphere, directly affecting the dynamics in ice and mixed-phase clouds, such as the formation and development of clouds and precipitation (Koehler et al., 2010;Twohy et al., 2009).

To date, many studies have been conducted to evaluate the direct radiative effect of dust aerosol using radiation schemes implemented in numerical models all over the world (Mallet et al., 2009;Nabat et al., 2015a;Ge et al., 2010;Hartmann et al., 2013;Huang et al., 2009;Bi et al., 2013;Liu et al., 2011a;Liu et al., 2011b;Huang, 2017). Recently, semi-direct effect of dust has been investigated in a few studies over different regions by applying various global and regional models (Tesfaye et al., 2015;Nabat et al., 2015b;Seigel et al., 2013). Unfortunately, due to the poor understanding on the dust-cloud-interactions in microphysics processes, quantifying the microphysical effect of dust remains as a difficult problem. Various ice nucleation parameterizations have been implemented into global models to estimate the importance of dust in atmospheric ice nucleation (Lohmann and Diehl, 2006;Karydis et al., 2011;Hoose et al., 2008;Zhang et al., 2014). However, most regional models are not capable of estimating the indirect effect of dust, and vary rare work has been done to assess the indirect effects of dust on the weather system, especially over East Asia, which is a major contributor to the global dust emission. Currently, only a few microphysics schemes

3

61 considering aerosol-cloud-interaction are implemented in regional models. In most of these microphysics schemes

62 only the cloud condensation nuclei (CCN) served by aerosols are considered (Perlwitz and Miller, 2010;Solomos et

63 al., 2011;Miller et al., 2004), while IN are not treated or represented by a prescribed IN distribution (Chapman et al.,

64 2009;Baró et al., 2015), and the production of ice crystals is simplified by a function of temperature or ice saturation.

65 In reality, however, the number of ice crystals that can form in the atmosphere is highly dependent on the number of

66 particles that can act as IN, and dust is the most abundant aerosols that can effectively serve as IN and affect the

67 formation and development of mixed-phase and ice clouds in the atmosphere. This effect should not be neglected in

68 numerical models, especially in the simulations over arid regions during strong wind events (DeMott et al.,

69 2003;Koehler et al., 2010;DeMott et al., 2015;Lohmann and Diehl, 2006;Atkinson et al., 2013).

70 In 2014, the aerosol-aware Thompson-Eidhammer microphysics scheme, which takes into account the aerosols

71 serving as CCN and IN, has been implemented into the Weather Research and Forecast (WRF) model, enabling the

72 model to explicitly predict the number concentration for cloud droplets and ice crystals (Thompson and Eidhammer,

73 2014). Therefore, the aerosol-aware Thompson-Eidhammer scheme is an ideal microphysics scheme for evaluating

74 the effect of dust in atmospheric ice nucleation processes. However, this scheme is not coupled with any aerosol model

75 in WRF-Chem, the Weather Research and Forecast model coupled with Chemistry. When the aerosol-aware

76 Thompson-Eidhammer microphysics scheme is activated, the model reads in pre-given climatological aerosol data

77 derived from the output of other global climate models, which introduces large errors into the estimation of the effects

78 of dust in microphysical processes. This problem can be solved by embedding a dust scheme into Thompson-

79 Eidhammer scheme, or couple the microphysics scheme with WRF-Chem. Compared with WRF, WRF-Chem

80 integrates various emission schemes and aerosol mechanisms for simulating the emission, transport, mixing, and

81 chemical transformation of aerosols simultaneously with the meteorology (Grell et al., 2013). Therefore, WRF-Chem

82 is more capable of producing a realistic aerosol field by comparing the performances of different emission schemes

83 or aerosol mechanisms.

84 In light of above, we aim to fully couple the aerosol-aware Thompson-Eidhammer microphysics scheme with the

85 Goddard Chemistry Aerosol Radiation and Transport (GOCART) model (Ginoux et al., 2001) in the WRF-Chem

86 modeling system in this study, enabling WRF-Chem to simultaneously simulate the effect of dust aerosol in ice

87 nucleation processes during simulations. Based upon the implementation, the performance of the coupled GOCART-

88 Thompson microphysics scheme in simulating the ice nucleation process involving dust particles was validated and

89 the role that East Asian dust plays in the ice nucleation process in the atmosphere was further investigated.

90 The remainder of the manuscript is presented as follows. Section 2 provides a description of the model including the

91 implementation work for coupling the aerosol-aware Thompson-Eidhammer microphysics scheme and the GOCART

92 aerosol model in WRF-Chem, followed by the model configurations for numerical simulations in section 3. Section 4

93 presents the observational data used to validate the performance of the GOCART-Thompson microphysics scheme.

94 Section 5 is the results and discussion, followed by the conclusions in section 6.

95

2 Model description

97 WRF-Chem is an online-coupled regional modeling system, which means that it can simultaneously simulate the

98 meteorological field, the chemical field, and the interactions in between (Grell et al., 2013). The chemical model

99 contains several gas- and aerosol-phase chemical schemes. In this study, we focus on the GOCART model, a simple

100 aerosol model that will be used for dust simulation.

101

2.1 GOCART aerosol model

103 GOCART is an aerosol model for simulating major tropospheric natural-source aerosol components, such as sulfate,

104 mineral dust, black carbon, organic carbon, and sea-salt aerosols (Ginoux et al., 2001;Chin et al., 2000). It has been

105 implemented into WRF-Chem as a bulk aerosol scheme. GOCART is a simple aerosol scheme that can predict the

106 mass of aerosol components, but does not account for complex chemical reactions. Therefore, it is numerically

107 efficient in simulating aerosol transport, and thus applicable to cases without many chemical processes, especially

108 dust events. Typically it requires 40% to 50% more computational time by applying WRF-Chem run with GOCART

109 aerosol model than the standard WRF to produce the same period of simulation.

110 Shao's dust emission scheme model (Kang et al., 2011;Shao, 2004, 2001;Shao et al., 2011) is one of the dust emission

111 schemes in the GOCART aerosol, and has been demonstrated to exhibit superior performance in reproducing the dust

112 cycle over East Asia compared to other emission schemes (Su and Fung, 2015). The Shao's emission scheme was

113 updated in WRF-Chem since version 3.8 released in 2016 to produce five size bins for dust emission, with diameters

114 of < 2 μm, 2–3.6 μm, 3.6–6.0 μm, 6.0–12.0 μm, and 12.0–20.0 μm, and mean effective radii of 0.73 μm, 1.4 μm, 2.4

115 μm, 4.5 μm, and 8.0 μm.

116

117 **2.2 Aerosol-aware Thompson microphysics scheme**

118 The Thompson scheme is a bulk two-moment microphysics scheme that considers the mixing ratios and number

119 concentrations for five water species: cloud water, cloud ice, rain, snow and a hybrid graupel/hail category (Thompson

120 et al., 2004). The Thompson-Eidhammer scheme is an aerosol-aware version of the Thompson scheme (Thompson

121 and Eidhammer, 2014). It incorporates the activation of aerosols serving as cloud condensation nuclei and IN, and

122 therefore it explicitly predicts the number concentrations of CCN and IN, as well as the number concentrations of

123 cloud droplets and ice crystals. Hygroscopic aerosols that serve as cloud condensation nuclei are referred to as water-

124 friendly aerosols, and those non-hygroscopic ice-nucleating aerosols are referred to as ice-friendly aerosols. The cloud

125 droplets nucleate from explicit aerosol number concentrations using a look-up table for the activated fraction as

126 determined by the predicted temperature, vertical velocity, number of available aerosols, and pre-determined values

127 of the hygroscopicity parameter and aerosol mean radius.

128 The parameterization for condensation and immersion freezing in the aerosol-aware Thompson-Eidhammer

129 microphysics scheme was proposed in 2010 (DeMott et al., 2010, hereafter referred to as the DeMott2010 scheme)

130 based on combined data from field experiments at a variety of locations over 14 years. In the Demott2010

131 parameterization, the relationship between the number concentration of aerosol-friendly aerosols and ice nucleating

132 particles (INP) is as follows:

133
$$n_{IN,T_k} = a(273.16 - T_k)^b n_{aero}^{(c(273.16-T_k)+d)} \qquad (1)$$

134 where n_{IN,T_k} is the ice crystal number concentration at temperature of T_k; n_{aero} is the number concentration of ice-

135 friendly aerosols, and a, b, c, and d are constant coefficients equal to 5.94×10^{-5}, 3.33, 2.64×10^{-2}, and 3.33×10^{-3},

136 respectively. The parameterization was tested with various temperatures and number concentration of ice-friendly

137 aerosols, yielding a good performance in reproducing ice crystal number concentration under conditions of relatively

138 low mixing ratio of water vapor or low concentration of INP compared with field–experimental data. The relationship

139   between the simulated number concentrations of ice-friendly aerosols and INP is basically linear for concentrations

140   of both of under 1,000 #/cm^3 (DeMott et al., 2010).

141   The above parameterization was further developed in 2015 (DeMott et al., 2015, hereafter the DeMott2015 scheme)

142   for conditions of higher mixing ratio of water vapor or higher concentrations of ice crystals based on the latest data

143   from field and laboratory experiments. According to the updated observational data, INP concentration increases

144   exponentially with number concentration of ice-friendly aerosols, and existing aerosols with relatively low

145   concentrations (less than 1,000 #/cm^3) can produce a large number of INP (more than 100,000 #/cm^3). The updated

146   relationship between the number concentrations of ice-friendly aerosols and INP in the DeMott2015 parameterization

147   scheme is as follows.

148
$$n_{IN,T_k} = c_f n_{aero}^{\alpha(273.16-T_k)+\beta} \exp(\gamma(273.16 - T_k) + \delta) \qquad\qquad (2)$$

149   where α, β, γ, and δ are constant coefficients equal to 0, 1.25, 0.46, and -11.6, respectively. The calibration factor c_f

150   ranges from 1 to 6, and is recommended to be 3.

151   The number concentration of INP produced by the DeMott2015 scheme is much higher than that produced by the

152   DeMott2010 scheme, and the difference grows larger with decreasing temperature and increasing number

153   concentration of ice-friendly aerosols (DeMott et al., 2015). As the DeMott2015 scheme has been examined using

154   more comprehensive field– and laboratory–experimental data, we apply the DeMott2015 ice nucleation scheme in the

155   GOCART–Thompson microphysics scheme to be implemented, instead of the DeMott2010 scheme, in the default

156   aerosol-aware Thompson-Eidhammer microphysics scheme to simulate the ice nucleation involving dust.

157   Originally, the calibration factor c_f is set to be 3; the threshold temperature is set to be –20 °C. The ice nucleation

158   process is triggered once the relative humidity with respect to ice (RH$_i$) exceeds 105%. Furthermore, when the relative

159   humidity with respect to water (RH$_w$) is above 98.5%, it is counted as condensation and immersion freezing, and

160   calculated by DeMott2015 scheme; when RH$_w$ is below 98.5%, it is treated as deposition nucleation, and determined

161   by the parameterization of Phillips et al. (Phillips et al., 2008) is applied to count for deposition nucleation.

162   In addition, the freezing of deliquesced aerosols using the hygroscopic aerosol concentration is parameterized

163   following Koop et al. (Koop et al., 2000), with the background aerosol concentration set to be 1E5. For the Thompson-

164   Eidhammer scheme in WRF, the number concentrations of both water-friendly aerosols and ice-friendly aerosols are

165 pre-given in the initialization of the simulations, and are derived from the climatological data produced by global

166 model simulations in which particles and their precursors are emitted by natural and anthropogenic sources and

167 explicitly modeled with various size bins for multiple species of aerosols by the GOCART model. In the consequent

168 simulations, a fake aerosol emission is implemented by giving a variable lower boundary condition based on the initial

169 near-surface aerosol concentration and a simple mean surface wind for calculating a constant aerosol flux at the lowest

170 level in the model. The number concentrations of both water-friendly aerosols and ice-friendly aerosols are then

171 updated at every time step by summing up the fake aerosol emission fluxes and tendencies induced by aerosol-cloud-

172 interactions. The limitation of the current aerosol-aware Thompson-Eidhammer scheme is that the aerosol profile

173 generated from a fake emission cannot represent the realistic aerosol level all the time, especially over areas with

174 complex weathers, such as East Asia, leading to errors in quantifying the indirect effects of aerosols.

175 By coupling the GOCART aerosol model with the Thompson-Eidhammer microphysics scheme, it allows the model

176 to explicitly evaluate the indirect effect of natural-source aerosols on the basic of a relatively realistic emission

177 production, for instance, the effect of dust on ice nucleation during severe dust episodes or dust-intensive season.

178

3 Implementation of GOCART-Thompson microphysics scheme

180 To investigate the real-time indirect effects of dust aerosol over East Asia, a new treatment was implemented into

181 WRF-Chem to couple the GOCART aerosol model and the Thompson-Eidhammer microphysics scheme, namely

182 GOCART-Thompson microphysics scheme. To accomplish this, WRF-Chem version 3.8.1 has been modified in the

183 following three steps.

184

3.1 Upgraded GOCART aerosol model

186 Currently, the GOCART aerosol model generates only the mass concentration for aerosols but no number

187 concentrations. However, the number concentrations of aerosols are required for a microphysics scheme to evaluate

188 the indirect effects of aerosols. Therefore, modification was needed to provide information about the number

189 concentrations of aerosols from the mass concentration produced in GOCART aerosol model.

190   The aerosol mass concentration was converted into number concentration using the aerosol density and effective radius

191   for each size bin. Assuming that dust particles are spherical, the mass per dust particle (m_p, μg/#) for a size bin can

192   be approximated through the mean effective radius (r_{dust}, m) and density (ρ_{dust}, kg/m^3) for that size bin.

193     $$m_p = \rho_{dust} \times \frac{4}{3} \times \pi r_{dust}^3 \qquad\qquad (3)$$

194   The number concentration of dust particles N (#/kg) for size bin n at a grid point (i, j, k) is then calculated by the

195   following equation:

196     $$N(i, j, k, n) = C(i, j, k, n) / m_p \qquad\qquad (4)$$

197   where C(i, j, k, n) is the dust mass mixing ratio (μg/kg) for size bin n at grid point (i, j, k). Summing up the aerosol

198   number concentrations through all of the size bins gives a total dust number concentration, which will be passed into

199   the Thompson-Eidhammer microphysics scheme. Note that all of the dust particles are treated as ice-friendly aerosols

200   in this study and represented by a newly-introduction variable, ice –friendly aerosol produced by GOCART aerosol

201   model (GNIFA).

202     $$GNIFA(i, j, k) = \sum_{i=1}^{n} N(i, j, k, n) \qquad\qquad (5)$$

203

204   **3.2 GOCART-Thompson microphysics scheme**

205   This part of modification was to hoop up the GOCART aerosol model and the Thompson-Eidhammer microphysics

206   scheme.

207   Instead of reading in the pre-given climatological aerosol data, the initialization module of the Thompson-Eidhammer

208   microphysics scheme was modified to apply the bulk number concentration of ice-friendly aerosols produced by the

209   GOCART aerosol model for the calculation of the number concentration of ice nucleating particles

210   After the microphysical processes are finished for a particular time step, the tendency of the bulk aerosol number

211   concentration (ten_{dust}, #/kg/s) produced by the microphysics scheme is then passed into a wet scavenging scheme,

212   which will be described in detail in the following subsection, for the model to calculate the loss of aerosol mass due

213   to the microphysical processes within clouds, and update the aerosol mass field.

214

3.3 In-cloud wet scavenging

216 As no in-cloud scavenging is considered for dust aerosol in WRF-Chem, a new wet scavenging process was introduced

217 into WRF-Chem to calculate the loss of aerosol mass due to the microphysical processes within clouds using the

218 tendency of aerosol number concentration produced by the microphysics scheme. Assuming that the collection of dust

219 particles is proportional to the number concentration of dust particles, the fraction of dust particle for each size bin

220 (φ, %) can be calculated in the GOCART aerosol model:

221
$$\varphi(i, j, k, n) = \frac{N(i,j,k,n)}{GNIFA(i,j,k)} \qquad (6)$$

222 The tendency of ice-friendly aerosol is then distributed into each size bin and the loss of dust mass due to the

223 microphysical processes (*wetscav*, $\mu g/kg$) for a particular size bin n is calculated by the following equation:

224
$$wetscav(i, j, k, n) = ten_{dust}\ (i, j, k) \times \varphi(i, j, k, n) \times m_p \times dt \qquad (7)$$

225 where dt is the time step for the simulation.

226 The mass mixing ratio (C, $\mu g/kg$) for dust aerosol in a particular size bin n is then updated at the next time step:

227
$$C_{(i,j,k,n)}^{t+1} = C_{(i,j,k,n)}^{t} - wetscav_{(i,j,k,n)}^{t} \qquad (8)$$

228 Apart from the in-cloud scavenging, the below-cloud wet removal is calculated by the default wet deposition scheme

229 in the GOCART aerosol model, in which the wet removal of dust is removed by a constant scavenging factor when

230 there is a precipitation (Duce et al., 1991;Hsu et al., 2009).

231

4 Model configurations

233 A numerical experiment was conducted to examine the performance of the newly-implemented GOCART–Thompson

234 microphysics scheme in simulating the ice nucleation process induced by dust in the atmosphere. Two simulations

235 were conducted for the numerical test. One control run (CTRL) was conducted without dust and one test run (DUST)

236 was conducted with dust. According to the observations, the dust events in 2012 over East Asia were concentrated in

237 mid-March to late-April, and the satellite observations from mid-March to the end of April were available for model

238 validation; therefore, the simulation period was from March 9 to April 30, 2012, with the first eight days as "spin-up"

239 time. Only the results from March 17 to April 30, 2012 were used for the analysis. The final reanalysis data provided

240 by the United States National Center of Environmental Prediction with a horizontal resolution of one degree was used

241 for generating the initial and boundary conditions for the meteorological fields, and the simulations were re-initialized

242 every four days, with the aerosol field being re-cycled, which means that the output of the aerosol field from the

243 previous four-day run was used as the initial aerosol state for the subsequent four-day run. The integration time step

244 for the simulations was 90s.

245 Two nested domains were used for the simulations, as shown in Figure 1. The outer domain (domain 1) is in a

246 horizontal resolution of 27 km and covers the entire East Asia region. The inner domain (domain 2) is in a horizontal

247 resolution of 9 km and covers the entire central to East China. Both domains have 40 vertical layers, with the top layer

248 at 50 hPa. The locations of the two major dust sources, the Taklimakan Desert (TD) and the Gobi Desert (GD), are

249 marked in Figure 1.

250 The GOCART aerosol model was applied to simulate aerosol processes (Ginoux et al., 2001;Ginoux et al., 2004).

251 Shao's dust emission (Kang et al., 2011;Shao et al., 2011) with soil data from the United states Geological Survey

252 (Soil Survey Staff, 1993), which have been demonstrated to have good performance in reproducing dust emissions

253 over East Asia, was used to generate dust emission in the test run. No other aerosol emissions were considered in the

254 simulations. The newly–implemented GOCART–Thompson microphysics scheme. In the GOCART-Thompson

255 scheme, the deposition nucleation is determined by the parameterization of Phillips et al. (Phillips et al., 2008), the

256 freezing of deliquesced aerosols using the hygroscopic aerosol concentration is parameterized following Koop et al.

257 (Koop et al., 2000), with the background aerosol concentration set to be 1/L, and the condensation and immersion

258 freezing is parameterized by the DeMott2015 ice nucleation scheme. The new wet scavenging scheme was used for

259 in-cloud wet scavenging of aerosols due to microphysical processes.

260 Other important physical and chemical parameterizations applied for the simulations are as follows. The Mellor–

261 Yamada–Janjic (MYJ) turbulent kinetic energy scheme was used for the planetary boundary layer parameterization

262 (Janjić, 2002, 1994); the moisture convective processes were parameterized by the Grell-Freitas scheme (Grell and

263 Freitas, 2014); the short-wave (SW) and long-wave (LW) radiation budgets were calculated by the Rapid Radiative

264   Transfer Model for General Circulation (RRTMG) SW and LW radiation schemes (Mlawer et al., 1997;Iacono et al.,

265   2008); the gravitational settling and surface deposition were combined for aerosol dry deposition calculation (Wesely,

266   1989); a simple washout method was used for the below-cloud wet deposition of aerosols (Duce et al., 1991;Hsu et

267   al., 2006); and the aerosol optical properties were calculated based on the volume-averaging method (Horvath, 1998).

268

269 5 Observations

270 5.1 Surface PM$_{10}$ observations

271   The hourly observations of surface concentration of particulate matter with diameter smaller than 10 μm (PM$_{10}$) at ten

272   environmental monitoring stations located in or surrounding the dust source areas in East Asia were used to examine

273   the capability of the model in reproducing dust levels at the ground surface during the simulation period. The ten

274   stations (indicated by blue dots in Figure 1) were located in the following five cities:Jinchang, Gansu Province,

275   Yinchuan, Qinghai Province, Shizuishan, Ningxia Province, Baotou, Inner Mongolia, and Yan'an, Shaanxi Province,

276   with two stations in each city.

277

278 5.2 AERONET AOD observations

279   The AERONET program is a ground-based aerosol remote sensing network for measuring aerosol optical properties

280   at sites distributed around the globe. This program provides a long-term database of aerosol optical properties such as

281   aerosol extinction coefficient, single-scattering albedo, and aerosol optical depth (AOD) measured at various

282   wavelength. The observational data from two sites were available for comparison with the simulation results during

283   the simulation period in this study. One was Dalanzadgad located to the north of the Gobi Desert in Mongolia, and

284   the other was the Semi-Arid Climate and Environment Observatory of Lanzhou University (SACOL) located at

285   Lanzhou, Gansu Province, China. The exact locations of the two AERONET sites are depicted by the red triangles in

286   Figure 1. All of the measured data had passed the quality control standard level 2, with an uncertainty of ±0.01 (Holben

287   et al., 2001).

288

289 **5.3 Satellite data**

290 **5.3.1 Multi-angle Imaging SpectroRadiometer (MISR)**

291 The MISR instrument aboard the Terra platform of the United State National Aeronautics and Space Administration

292 (NASA) has been monitoring aerosol properties globally since 2000. It measures the aerosol properties in four narrow

293 spectral band centered at 443 nm, 555 nm, 670 nm, and 865 nm, due to which the aerosol properties even over highly

294 bright surfaces, such as deserts, can be retrieved (Martonchik et al., 2004;Diner et al., 1998). In this study, the AOD

295 data at 555 nm retrieved from the MISR level 3 products with a spatial resolution of 0.5° were used for comparison

296 with the spatial distribution of simulated AOD over East Asia during the investigated period.

297

298 **5.3.2 Moderate Resolution Imaging Spectroradiometer (MODIS)**

299 The MODIS instruments aboard Terra and Aqua platforms of NASA monitor Earth's surface and provide global high-

300 resolution cloud and aerosol optical properties at a near-daily interval (Kaufman et al., 1997).

301 To retrieve aerosol information over bright surfaces, the Deep Blue algorithm was developed to employ retrievals

302 from the blue channels of the MODIS instruments, at which wavelength the surface reflectance is very low, such that

303 the presence of aerosol can be detected by increasing total reflectance and enhanced spectral contrast (Hsu et al., 2006).

304 By applying this algorithm, the AOD values at wavelengths of 214 nm, 470 nm, 550 nm, and 670 nm over bright

305 surfaces can be retrieved. In this study, the MODIS level 2 AOD data at 550 nm with a spatial resolution of 10 km

306 were used for comparison with the simulated AOD during the simulation period.

307

308 **5.3.3 Cloud-Aerosol Lidar and Infrared Pathfinder Satellite Observation (CALIPSO)**

309 The Cloud-Aerosol Lidar and Infrared Pathfinder Satellite, which is aboard the Aqua platform of NASA, combines

310 an active Light Detection and Ranging (LIDAR) instrument with passive infrared and visible imagers to probe the

311 vertical structure and properties of thin clouds and aerosols around the globe (Vaughan et al., 2004). It aims to fill

312 existing gaps in the ability to measure the global distribution of aerosols and cloud properties, and provides three-

313 dimensional perspectives of how clouds and aerosols form, evolve, and affect weather and climate. It measures high-

314   resolution vertical profiles of aerosol and cloud extinction coefficient globally at wavelengths of 532nm and 1064 nm.

315   The atmospheric IWC is derived from the observational cloud extinction coefficients at 532 nm (Winker et al., 2009).

316   In this study, the vertical profiles of CALIPSO IWC with a horizontal resolution of 5 km and vertical resolution of 60

317   m were applied to verify the performance of the model in simulating the vertical distribution of atmospheric IWC.

318

319   **6 Results and model validation**

320   **6.1 Dust over East Asia**

321   The time series of daily average dust load over the entire East Asia region (domain 1) during the simulation period is

322   shown in Figure 2a. In total four dust events occurred during the simulation period, lasting from March 18 to 25,

323   March 30 to April 7, April 9 to 19, and April 22 to 29, 2012. The case from April 22 to 29 was the most significant

324   one, with daily dust load that double as the other cases. The fraction of daily dust load for each size bin is also shown

325   in Figure 2a. The dust particles in the fourth and fifth bins with effective diameters ranging from 6 to 20 μm account

326   for around 60% of the total mass of dust aerosols, and dust particles with diameters smaller than 6 μm account for

327   around 40% of the total mass of dust aerosols.

328   The number concentration of dust particles over East Asia were vertically integrated to obtain the number density of

329   dust particles. As shown in Figure 2b, the time series of the daily average number density of dust particles over East

330   Asia during the simulation period shows a similar distribution as that for dust load; the noteworthy distinction between

331   the two time series lies in the fraction of each size bin. The two size bins with the smallest diameters (no larger than

332   3.6 μm) account for over 80% of the total number of dust particles, and the particles with diameters smaller than 6 μm

333   account for over 95% of the total number of dust particles, indicating that the smallest dust particles are the main

334   source of ice-friendly aerosol to serve as IN in the atmosphere.

335

336   **6.1.1 Surface PM$_{10}$ concentration**

337   To evaluate the performance of WRF-Chem in reproducing dust emissions over East Asia, the simulated surface PM$_{10}$

338   concentrations were compared with the observations from the ten environmental monitoring stations located near dust

14

339   sources and downwind areas (described in Section 5.1). The time series of the observed and simulated surface PM_{10}

340   concentrations during the simulation period are shown in Figure 3. Note that the simulated PM_{10} concentration were

341   extracted from the nearest grid point to the geographical coordinates of the stations. The stations in the same city were

342   assigned into one group, thus here were five groups in Figure 3. Overall, the model shows a good performance in

343   simulating the dust cycle at different locations, with evolution and magnitude of the daily mean PM_{10} concentration

344   well captured at most of the stations. The model tends to produce lower surface PM10 concentration than those

345   observed, as no other emissions were considered in the simulations. However, the dust events on March 21 and April

346   26 were overestimated by the model at one station in Jinchang (Figure 3e), both stations in Shizuishan (Figure 3c and

347   d) and Yinchuan (Figure 3i and j).

348   The performance statistics were computed from the daily average simulated PM10 concentration from DUST and the

349   corresponding observations, as shown in Table 1. The model tends to produce lower surface PM_{10} concentrations than

350   those observed, as no other emissions were considered in the simulations. The mean bias (MB) ranged from -108.73

351    $\mu g/m^3$ to 72.46 $\mu g/m^3$, with a mean over all the stations of -18.84 $\mu g/m^3$. The mean error (ME) ranged from 46.07

352    $\mu g/m3$ to 155.83 $\mu g/m3$, with a mean over all of the stations of 107.24 $\mu g/m^3$. The root mean squared error (RMSE)

353   ranged from 64.78 $\mu g/m^3$ to 317.73 $\mu g/m^3$, with a mean over all of the stations of 181.28 $\mu g/m^3$. The relatively large

354   values of the MB, ME and RMSE are mainly attributed to the fact that no other aerosol emissions were considered in

355   the simulations other than dust, while the surface PM_{10} concentration at the monitoring stations is influenced by

356   aerosols emitted from other sources, such as anthropogenic emissions. The correlation coefficient (r) ranged from 0.59

357   to 0.87, with an average for all of the stations of 0.70. The comparisons between the observed and simulated surface

358   PM_{10} concentration indicates that the model is capable of reproducing the surface dust concentration reasonably during

359   dust events over East Asia.

360

361   **6.1.2 AOD time series**

362   To examine the performance of the model in reproducing the column sum of dust in the atmosphere, the simulated

363   AOD values were compared with observations measured at two AERONET sites during the simulation period, as

364   shown in Figure 4.

365   The site at Dalanzadgad (Figure 4a) is located in Mongolia to the north of the Gobi Desert. Overall, the evolution and

366   magnitude of the AOD time series at Dalanzadgad were reasonably reproduced by the model during the simulation

367   period, despite the fact that the simulated AOD was overestimated at the end of March and in mid-April compared to

368   the observed values.

369   SACOL (Figure 4b) is a site located in Lanzhou, Gansu Province, which is a typical downwind area for dust in China.

370   The model showed a good performance in reproducing the time series of AOD at SACOL during the entire simulation

371   period, with evolution and magnitude of AOD well captured.

372

6.1.3 AOD spatial distribution

374   The spatial distribution of monthly mean simulated AOD was also compared with observed values from MODIS and

375   MISR products. Note that the high AOD values observed at North, East, South China and part of Southeast Asia are

376   attributed to the abundant anthropogenic emissions, while those high values in the circle area are mostly due to dust

377   events. The region with high AOD values in the west part of the circled area is TD, and the region with relatively

378   lower AOD in the east part of the circled area is GD. The AOD observed by MODIS showed high values at the dust

379   source region in both March and April of 2012, as shown in Figures 5a and b. The mean observed AOD over GD was

380   lower than that over TD in both March and April, and the mean observed AOD was higher in April than in March

381   over both dust source areas. The spatial patterns of AOD observed by MISR are similar to MODIS, with comparable

382   mean values over GD. However, the mean AOD values over TD observed by MISR are 36% and 40% lower than

383   those by MODIS, respectively (Figure 5c and d).

384   The spatial patterns for the mean simulated AOD were similar to the observed values in both months but closer to

385   those from MODIS, as shown in Figures 5e and f. The model shows a good capability in capturing the spatial

386   characteristics of the AOD over the dust source areas. For example, the mean observed AOD was higher in the

387   southern part of TD than that in the northern part in March, and showed an increase from March to April over GD,

388   both of which were captured by the model. The values of the mean simulated AOD over the Gobi Desert (0.33 for

389   March and 0.39 for April) are comparable to the observational values from both MODIS (0.30 for March and 0.32 for

390   April) and MISR (0.31 for March and 0.34 for April), but the mean simulated AOD over TD (0.54 for March and 0.64

16

391   for April) are between the values of the MISR observations (0.72 for March and 0.88 for April) and the MODIS

392   observations (0.46 for March and 0.53 for April).

393   In summary, it was demonstrated that the dust emissions simulated by WRF-Chem are reliable for further analysis by

394   the comparison between the simulation results and the observations for surface PM_{10} concentrations, as well as the

395   temporal and spatial distributions of AOD values.

396

397   6.2 Cloud ice over East Asia

398   Dust particles are effective IN and play an important role in ice nucleation in the atmosphere under appropriate

399   conditions. With the large number of IN served by dust particles emitted into the atmosphere, an increase in the number

400   of ice crystals is expected in the results from DUST compared with those from CTRL, after taking into account the

401   effects of dust particles in the GOCART–Thompson microphysics scheme. Figure 6 shows the overall comparison

402   between the simulated cloud ice mixing ratio and ice crystal number concentration at each simulated data point (at

403   all model grids at hourly intervals) from CTRL and DUST during the entire simulation period.

404   As expected, the model produces a much higher cloud ice mixing ratio (Figure 6a) and ice crystal number

405   concentration (Figure 6b) in DUST. The simulated cloud ice mixing ratio produced in CTRL is lower than 2 μg/kg at

406   most data points during the simulation period, whereas the data points with simulated ice mixing ratio higher than 2

407   μg/kg are substantially increased in the output of DUST. Similarly, the simulated ice crystal number concentration

408   produced in CTRL is lower than 0.5×10^6 #/kg at most data points during the simulation period, by contrast, the

409   simulated ice crystal number concentration number concentration is higher than 0.5×10^6 #/kg at over a half of total

410   data points in DUST. The substantial increase of simulated cloud ice mixing ratio and ice crystal number concentration

411   indicates that the enhancement of ice nucleation process induced by dust is successfully reproduced by the newly-

412   implemented GOCART-Thompson microphysics scheme during the simulation period.

413

414   6.2.1 Spatial distribution of ice water path (IWP)

415 The spatial distributions of the simulated IWP and ice crystal number density from CTRL and DUST in Figure 7

416 further demonstrate the enhancement in cloud ice due to dust over East Asia. The IWP produced by CTRL was lower

417 than 1 g/m^2 over the entire East Asia Region (Figure 7a). After considering the effect of dust in the ice nucleation

418 process, the IWP produced by DUST increased substantially over the entire region, especially over dust sources and

419 downwind areas, with values as high as 10 g/m^2 (Figure 7b and c). The mean IWP averaged over the domain during

420 the simulation period was 9.15 g/m^2 for DUST, and 0.70 g/m^2 for CTRL. As shown in Figures 7d–f, the spatial pattern

421 for the enhancement of ice crystal number density over East Asia was similar with that for the IWP. The mean ice

422 crystal number density averaged over the domain during the simulation period was 2.79×10^8 $/m^2$ for DUST, and

423 6.38×10^6 $/m^2$ for CTRL.

424 The IWP and ice crystal number density were increased by more than one order of magnitude over vast areas of East

425 Asia upon considering the effect of dust in the ice nucleation process in the simulation, and such effect can reach as

426 far as the South China Sea at the southern part of the simulation domain (Figure 7b and 7e). During dust season, the

427 outbreak of cold high system over northeast Asia can bring quantitative dust aerosol down to the South China Sea or

428 even further. In such cases, strong northwestlies swept across the entire China, and brought large amount of dust,

429 especially fine particles, from source areas to the south border of the domain. Besides, the water vapor mixing ratio

430 over South China Sea can be several times as that over north China. Large amount of ice nuclei transported by winds,

431 combining with abundant water vapor, results in a substantial enhancement in the formation of ice crystals over the

432 area at the southern part of the simulation domain. The larger fraction of fine particles in the dust plumes that reach

433 this area results in a much higher enhancement of ice crystal number concentration than the mass of ice crystals.

434

435 **6.2.2 IWC during dust events**

436 The vertical profile of the simulated IWC was also compared with the observation from CALIPSO during dust events.

437 As mentioned in section 5.1, a total of four dust events occurred during the simulation period, lasting from March 18

438 to 25, March 30 to April 7, April 9 to 19, and April 22 to 28, 2012. As shown in Figures 8 and 9, the performance of

439 the model in simulating the vertical profile of IWC was evaluated by comparing the observations measured at 06 UTC

440 on March 21, 18 UTC on April 1, 18 UTC on April 9, and 05 UTC on April 23, 2012 with the simulated profiles at

441 the same hour.

442   CALIPSO measures the global distribution of aerosol and cloud properties by LIDAR, which uses a laser to generate

443   visible light with a wavelength of 1 μm or less to detect small particles or droplets in the atmosphere. Therefore,

444   CALIPSO instruments are more sensitive to tenuous ice clouds and liquid clouds composed of small particles or

445   droplets, which are invisible to instruments using signals of near-infrared or infrared wavelength to detect clouds.

446   Moreover, the LIDAR signal is attenuated rapidly in optically dense clouds that the infrared or near-infrared signals

447   can easily penetrate(Winker et al., 2010). As a result, the CALIPSO observations of IWC are mostly at the locations

448   where the temperatures is lower than −40 °C and the altitude is greater than 6 km poleward to 12 km equatorward,

449   and mostly those without precipitating ice. Given the above considerations, the simulated IWC profiles compared with

450   the CALIPSO observations are referred to as only cloud ice in this section.

451   The simulated dust load over East Asia at 06 UTC on March 21, 2012 is shown in Figure 8a, in which the dust covered

452   vast areas from West to East China between 35°N and 45°N, and the orbit of the satellite passed through the area with

453   heavy dust load at around 100°E. Along the satellite orbit, the abundant dust particles were transported to as high as

454   10 km aloft (Figure 8c). At this time, a high concentration of IWC was observed along the satellite orbit at an altitude

455   of around 10 km between 30°N and 45°N (Figure 8e). The simulation result from CTRL (Figure 8g) shows that the

456   model produces some ice cloud at altitude of 9–10 km between 35°N and 45°N, but with much lower IWC compared

457   to the observations. Nevertheless, by considering the effect of dust on ice nucleation process in DUST, it results in a

458   much higher IWC at altitude of 9–10 km between 35°N and 45°N (Figure 8i), which is much more consistent with the

459   observations. The comparison between the simulation results from CTRL and DUST indicates that the high IWC

460   observed by the satellite between 30°N and 35°N might be unrelated to microphysical processes, but instead due to

461   strong convective motions over South China.

462   On April 1, 2012, Central to East China was covered by a thick dust plume, and the orbit of the satellite passed between

463   25°N and 43°N along 120°E at 18 UTC (Figure 8b). Dust particles were distributed vertically from the surface to over

464   8 km along the satellite orbit (Figure 8d). A band of high IWC was observed by the satellite at altitude of 5 km to 10

465   km between 33°N and 44°N (Figure 8f), which was barely reproduced in the results of the CTRL run without dust. In

466   contrast, the observed band of high IWC was reproduced by the model in DUST with much more consistent location

467   and magnitude (Figure 8j).

468   At 18 UTC on April 9, 2012, the satellite was scanning the dust source over GD, which was covered by a thick dust

469   plume between 35°N and 45°N (Figure 10a), with dust particles lifted up to 10 km above the surface (Figure 9c). High

470   concentration of IWC was observed by the satellite at altitude from 5 km to 11 km between 30°N and 45°N (Figure

471   9e). In this case, the model reproduced the high concentration of IWC at the observed location in the results from both

472   CTRL and DUST, although the IWC was significantly underestimated in the results from CTRL (Figure 9g), while it

473   was better reproduced in the results from DUST (Figure 9j).

474   Similar to the previous cases, the satellite was scanning along east coast of China at 05 UTC on April 23, 2012, when

475   a dust plume was arriving from the dust sources and affecting areas between 35°N and 45°N (Figure 9b), and dust

476   particles were distributed vertically from the surface to 10 km along the scanning track of the satellite (Figure 9d).

477   Along the orbit of the satellite, two bands with high IWC were observed at altitudes between 5 km and 12 km, one is

478   located between 30°N and 37°N, and the other is located between 40°N and 45°N (Figure 9f). In the results from

479   CTRL, the model reproduced the bands of high IWC at the correct locations, but with substantially lower values

480   (Figure 9h); however, upon taking into account the effect of dust in the GOCART-Thompson microphysics scheme,

481   the bands of high IWC were well reproduced by the model, with much more consistent values (Figure 9j).

482   By comparing the satellite-observational and simulated vertical profiles of IWC during the various dust events, it was

483   demonstrated that by considering the effects of dust on ice nucleation process, the model reproduces the enhancement

484   of IWC clouds in the mid- to upper troposphere by taking in to account the effect of dust in the ice nucleation process,

485   which substantially improves the simulation of cloud ice.

486

487   **6.2.3 Mean vertical profiles of IWC**

488   The mean profiles of the observed IWC, as well as the simulated IWC from CTRL and DUST for the four dust events

489   discussed in Section 6.2.2, are shown in Figure 10. Note that the "mean profile" of IWC is the average over the

490   available data points for the IWC along the orbit of the satellite between 30°N to 45°N for each of the dust events

491   shown in Figures 8 and 9.

492   Compared with the results from CTRL, the vertical profile of the simulated IWC was substantially improved in DUST

493   for each dust event, with the enhancement of the ice nucleation process well captured by the GOCART-Thompson

494 microphysics scheme. However, there were still discrepancies between observations and the simulation results from

495 DUST, the magnitudes of the vertical IWC produced by the model were always lower than the observed values.

496 For the cases on March 21 and April 1, the peaks of IWC were observed at 9.5 km and 8 km, respectively, whereas

497 the simulated peak of IWC were located at 8 km and 7.5 km, respectively, with lower peak values. The lower peak

498 value for the case on March 21 was due to the missing of the high IWC observed between 30°N to 45°N in the

499 simulation results (Figure 8e and i), while the lower peak value for the case on April 1 was due to the underestimation

500 of the IWC around 35°N (Figure 8f and j). The locations of the peaks of simulated IWC for the cases on April 9 and

501 April 23 were more consistent with the observed peaks, but still possessed lower values due to the missing or

502 underestimation of high IWC with respect to the observations.

503

6.3 Sensitivity test and discussion

505 As discussed in Section 6.2.3, the simulation of cloud ice is greatly improved by considering the enhancement of ice

506 nucleation process induced by dust, which is well captured by the GOCART–Thompson microphysics scheme.

507 However, the IWC is still underestimated by the model during dust events. To determine the reason for this limitation,

508 numerical experiments were performed to investigate the sensitivity of simulated IWC to the parameters of the ice

509 nucleation parameterization in the GOCART–Thompson microphysics scheme.

510

6.3.1 Calibration factor c_f

512 The calibration factor c_f is an empirical tuning coefficient derived from observational data from field and laboratory

513 experiments. It ranges from 1 to 6, and recommended to be 3 (DeMott et al., 2015), which was applied in the previous

514 simulations. Three other experiments were conducted to investigate the sensitivity of the simulated IWC to c_f values

515 ranging from 3 to 6.

516 The mean profiles of IWC from simulation results were compared with the CALIPSO observations for the dust events

517 discussed in Section 6.2.2 and 6.2.3, as shown in Figure 11. For the cases on March 21 and April 1, changing c_f did

518 not result in an increase of IWC; instead, the simulated IWC remained consistent for c_f values varying from 3 to 6.

519   For the case on April 9, the simulated IWC increased between 6 km and 9 km and was closer ro the observed profile

520   when c_f was equal to 4 and 5; however, when c_f was set to 3 and 6, the simulated IWC was lower than that obtained

521   with c_f values of 4 or 5.

522   For the case on April 23, two peaks were observed in the profiles of simulated IWC, located at 7 km and 10 km. The

523   simulated IWC remained unchanged with c_f values varying from 3 to 6 for the peak at 10 km, but increased upon

524   changing the c_f from 3 to 4, and remained the same upon changing the c_f from 5 and 6 for the peak. The peak of the

525   simulated IWC at 7 km should correspond to the observed peak between 6 km to 8 km, which was slightly

526   overestimated by the model.

527   In summary, increasing the calibration factor c_f from 3 to 6 does not necessarily lead to a significant variation in the

528   simulated IWC during dust events, and the model achieves a relatively better performance in reproducing the profile

529   of IWC when the c_f is set to 4 or 5.

530   As ice nucleation occurs only in a super-saturated atmosphere with respect to water vapor, the ice nucleation process

531   would be terminated in the GOCART-Thompson microphysics scheme when the environmental RH_i is lower than the

532   threshold RH_i, which was set to 105% for the simulations in this study. The consistency in the simulated IWC with

533   increasing c_f for the cases in Figure 11 indicates that in these cases, the environmental RH_i had already reached below

534   105% when c_f was set to 3, meaning that the water vapor available for freezing into ice crystals has been consumed

535   up with c_f equal to 3, therefore, increasing c_f could not lead to a further increase in simulated IWC. Given the above,

536   lowering the threshold RH_i might result in an enhancement of the ice nucleation process as well as the simulated IWC,

537   which will be discussed in the following section.

538

539   **6.3.2 Threshold of relative humidity**

540   In this study, the threshold relative humidity to trigger the ice nucleation process in the simulation was originally set

541   to 105%, which was selected for the central lamina condition in the laboratory experiments to derive the DeMott2015

542   ice nucleation scheme (DeMott et al., 2015). However, as reported in other studies, the number of ice nucleating

543 particles starts to rise when the relative humidity exceeds 100% (DeMott et al., 2011). Therefore, a sensitivity

544 experiment was carried out to investigate the response of simulated IWC to lower threshold relative humidity.

545 The mean profiles of IWC from the simulation results were compared with the CALIPSO observations for the

546 aforementioned dust events, as shown in Figure 12. With the threshold relative humidity lowered to 100%, the

547 simulated IWC showed an increase throughout the vertical profile with the most significant increase at the peaks,

548 suggesting more consistency with the observations for all of the dust events, except the one on April 1. In the case on

549 April 1, the simulated IWC increased at lower altitudes than the observed peak, but slightly decreased right at the peak

550 with lowering the threshold relative humidity to 100%. Overall, the simulation of IWC during dust events was

551 significantly improved by lowering the threshold relative humidity from 105% to 100%.

552

553 **7 Conclusions**

554 A new treatment, the GOCART–Thompson scheme, was implemented into WRF-Chem to couple the GOCART

555 aerosol model to the aerosol-aware Thompson-Eidhammer microphysics scheme. By applying this newly-

556 implemented microphysics scheme, the effect of dust on the ice nucleation process by serving as IN in the atmosphere

557 can be quantified and evaluated. Numerical experiments, including a control run without dust and a test run with dust,

558 were then carried out to evaluate the performance of the newly–implemented GOCART–Thompson microphysics

559 scheme in simulating the effect of dust on the content of cloud ice over East Asia during a typical dust-intensive period,

560 by comparing the simulation results with various observations.

561 Based on the GOCART aerosol model the model reproduced dust emission reasonably well, by capturing the evolution

562 and magnitude of surface PM_{10} concentration at the locations of various environmental monitoring stations and the

563 AOD at two AERONET sites. The spatial patterns of the mean AOD over East Asia during the simulation period were

564 also consistent with satellite observations.

565 The effect of dust on the ice nucleation process was then quantified and evaluated in the GOCART–Thompson

566 microphysics scheme. Upon considering the effect of dust in the simulation, the simulated ice water mixing ratio and

567 ice crystal number concentration over East Asia were one order of magnitude higher than those simulated without

568 dust, with the most significant enhancements located over dust source regions and downwind areas.

23

569   By comparing the simulated IWP averaged over East Asia during the simulation period with MODIS observations, it

570   was demonstrated that the IWP including cloud ice and precipitating ice was reasonably reproduced by the model over

571   most areas of East Asia, although slightly underestimated. The results from the simulation run with dust were more

572   consistent with the observations.

573   Comparison between the vertical profiles of the satellite-observed and simulated IWC during various dust events

574   indicated that the enhancement of cloud ice induced by abundant dust particles serving as IN is well captured by the

575   GOCART–Thompson microphysics scheme, with the results from the simulation with dust much more consistent with

576   the satellite–observations, although the IWC is generally underestimated by the model.

577   Sensitivity experiments revealed that the simulated IWC was not very sensitive to the calibration factor defined in the

578   DeMott2015 ice nucleation scheme, but the model delivered a slight better performance in reproducing the IWC when

579   the calibration factor was set to 3 or 4. However, the simulated IWC was sensitive to the threshold relative humidity

580   to trigger the ice nucleation process in the model and was improved upon lowering the threshold relative humidity

581   from 105% to 100%.

582

594

595 **References**

596 Atkinson, J. D., Murray, B. J., Woodhouse, M. T., Whale, T. F., Baustian, K. J., Carslaw, K. S., Dobbie, S., O'sullivan,
597 D., and Malkin, T. L.: The importance of feldspar for ice nucleation by mineral dust inmixed-phase clouds, Nature,
598 498, 355, 2013.

599 Baró, R., Jiménez-Guerrero, P., Balzarini, A., Curci, G., Forkel, R., Grell, G., Hirtl, M., Honzak, L., Langer, M., and
600 Pérez, J. L.: Sensitivity analysis of the microphysics scheme in WRF-Chem contributions to AQMEII phase 2,
601 Atmospheric Environment, 115, 620-629, 2015.

602 Bi, J., Huang, J., Fu, Q., Ge, J., Shi, J., Zhou, T., and Zhang, W.: Field measurement of clear-sky solar irradiance in
603 Badain Jaran Desert of Northwestern China, Journal of Quantitative Spectroscopy and Radiative Transfer, 122, 194-
604 207, 2013.

605 Chapman, E. G., Gustafson Jr, W., Easter, R. C., Barnard, J. C., Ghan, S. J., Pekour, M. S., and Fast, J. D.: Coupling
606 aerosol-cloud-radiative processes in the WRF-Chem model: Investigating the radiative impact of elevated point
607 sources, Atmospheric Chemistry and Physics, 9, 945-964, 2009.

608 Chin, M., Rood, R. B., Lin, S.-J., Müller, J.-F., and Thompson, A. M.: Atmospheric sulfur cycle simulated in the
609 global model GOCART: Model description and global properties, 2000.

610 DeMott, P. J., Sassen, K., Poellot, M. R., Baumgardner, D., Rogers, D. C., Brooks, S. D., Prenni, A. J., and
611 Kreidenweis, S. M.: African dust aerosols as atmospheric ice nuclei, Geophysical Research Letters, 30, 2003.

612 DeMott, P. J., Prenni, A. J., Liu, X., Kreidenweis, S. M., Petters, M. D., Twohy, C. H., Richardson, M., Eidhammer,
613 T., and Rogers, D.: Predicting global atmospheric ice nuclei distributions and their impacts on climate, Proceedings
614 of the National Academy of Sciences, 107, 11217-11222, 2010.

615 DeMott, P. J., Möhler, O., Stetzer, O., Vali, G., Levin, Z., Petters, M. D., Murakami, M., Leisner, T., Bundke, U., and
616 Klein, H.: Resurgence in ice nuclei measurement research, Bulletin of the American Meteorological Society, 92, 1623-
617 1635, 2011.

618 DeMott, P. J., Prenni, A. J., McMeeking, G. R., Sullivan, R. C., Petters, M. D., Tobo, Y., Niemand, M., Möhler, O.,
619 Snider, J. R., and Wang, Z.: Integrating laboratory and field data to quantify the immersion freezing ice nucleation
620 activity of mineral dust particles, Atmospheric Chemistry and Physics, 15, 393-409, 2015.

621 Diner, D. J., Barge, L. M., Bruegge, C. J., Chrien, T. G., Conel, J. E., Eastwood, M. L., Garcia, J. D., Hernandez, M.
622 A., Kurzweil, C. G., and Ledeboer, W. C.: The Airborne Multi-angle Imaging SpectroRadiometer (AirMISR):
623 instrument description and first results, IEEE Transactions on Geoscience and Remote Sensing, 36, 1339-1349, 1998.

624 Duce, R., Liss, P., Merrill, J., Atlas, E., Buat-Menard, P., Hicks, B., Miller, J., Prospero, J., Arimoto, R., and Church,
625 T.: The atmospheric input of trace species to the world ocean, Global biogeochemical cycles, 5, 193-259, 1991.

626 Ge, J., Su, J., Ackerman, T., Fu, Q., Huang, J., and Shi, J.: Dust aerosol optical properties retrieval and radiative
627 forcing over northwestern China during the 2008 China-US joint field experiment, Journal of Geophysical Research:
628 Atmospheres, 115, 2010.

629 Ginoux, P., Chin, M., Tegen, I., Prospero, J. M., Holben, B., Dubovik, O., and Lin, S. J.: Sources and distributions of
630 dust aerosols simulated with the GOCART model, Journal of Geophysical Research: Atmospheres, 106, 20255-20273,
631 2001.

632   Ginoux, P., Prospero, J. M., Torres, O., and Chin, M.: Long-term simulation of global dust distribution with the

633   GOCART model: correlation with North Atlantic Oscillation, Environmental Modelling & Software, 19, 113-128,

634   2004.

635   Grell, G., Peckham, S., Fast, J., Singh, B., Easter, R., Gustafson, W., Rasch, P., Wolters, S., Barth, M., and Pfister, G.:

636   WRF-Chem V3. 5: A summary of status and updates, EGU General Assembly Conference Abstracts, 2013, 11332.

637   Grell, G. A., and Freitas, S. R.: A scale and aerosol aware stochastic convective parameterization for weather and air

638   quality modeling, Atmos. Chem. Phys, 14, 5233-5250, 2014.

639   Hansen, J., Sato, M., and Ruedy, R.: Radiative forcing and climate response, Journal of Geophysical Research:

640   Atmospheres, 102, 6831-6864, 1997.

641   Hartmann, D., Tank, A., and Rusticucci, M.: IPCC fifth assessment report, climate change 2013: The physical science

642   basis, IPCC AR5, 31-39, 2013.

643   Holben, B., Tanre, D., Smirnov, A., Eck, T., Slutsker, I., Abuhassan, N., Newcomb, W., Schafer, J., Chatenet, B., and

644   Lavenu, F.: An emerging ground-based aerosol climatology: Aerosol optical depth from AERONET, Journal of

645   Geophysical Research: Atmospheres, 106, 12067-12097, 2001.

646   Hoose, C., Lohmann, U., Erdin, R., and Tegen, I.: The global influence of dust mineralogical composition on

647   heterogeneous ice nucleation in mixed-phase clouds, Environmental Research Letters, 3, 025003, 2008.

648   Horvath, H.: Influence of atmospheric aerosols upon the global radiation balance, Atmospheric particles, 5, 62-63,

649   1998.

650   Hsu, N. C., Tsay, S.-C., King, M. D., and Herman, J. R.: Deep blue retrievals of Asian aerosol properties during ACE-

651   Asia, IEEE Transactions on Geoscience and Remote Sensing, 44, 3180-3195, 2006.

652   Hsu, S. C., Liu, S. C., Arimoto, R., Liu, T. H., Huang, Y. T., Tsai, F., Lin, F. J., and Kao, S. J.: Dust deposition to the

653   East China Sea and its biogeochemical implications, Journal of Geophysical Research: Atmospheres, 114, 2009.

654   Huang, J., Fu, Q., Su, J., Tang, Q., Minnis, P., Hu, Y., Yi, Y., and Zhao, Q.: Taklimakan dust aerosol radiative heating

655   derived from CALIPSO observations using the Fu-Liou radiation model with CERES constraints, Atmospheric

656   Chemistry and Physics, 9, 4011-4021, 2009.

657   Huang, J.: Emission, transport, and radiative effects of mineral dust from the Taklimakan and Gobi deserts:

658   comparison of measurements and model results, Atmos. Chem. Phys, 1680, 7324, 2017.

659   Iacono, M. J., Delamere, J. S., Mlawer, E. J., Shephard, M. W., Clough, S. A., and Collins, W. D.: Radiative forcing

660   by long-lived greenhouse gases: Calculations with the AER radiative transfer models, Journal of Geophysical

661   Research: Atmospheres, 113, 2008.

662   Janjić, Z. I.: The step-mountain eta coordinate model: Further developments of the convection, viscous sublayer, and

663   turbulence closure schemes, Monthly Weather Review, 122, 927-945, 1994.

664   Janjić, Z. I.: Nonsingular implementation of the Mellor–Yamada level 2.5 scheme in the NCEP Meso model, NCEP

665   office note, 437, 61, 2002.

666   Kang, J. Y., Yoon, S. C., Shao, Y., and Kim, S. W.: Comparison of vertical dust flux by implementing three dust

667   emission schemes in WRF/Chem, Journal of Geophysical Research: Atmospheres, 116, 2011.

26

668 Karydis, V., Kumar, P., Barahona, D., Sokolik, I., and Nenes, A.: On the effect of dust particles on global cloud
669 condensation nuclei and cloud droplet number, Journal of Geophysical Research: Atmospheres, 116, 2011.

670 Kaufman, Y., Tanré, D., Remer, L. A., Vermote, E., Chu, A., and Holben, B.: Operational remote sensing of
671 tropospheric aerosol over land from EOS moderate resolution imaging spectroradiometer, Journal of Geophysical
672 Research: Atmospheres, 102, 17051-17067, 1997.

673 Koehler, K., Kreidenweis, S., DeMott, P., Petters, M., Prenni, A., and Möhler, O.: Laboratory investigations of the
674 impact of mineral dust aerosol on cold cloud formation, Atmospheric Chemistry and Physics, 10, 11955-11968, 2010.

675 Koop, T., Luo, B., Tsias, A., and Peter, T.: Water activity as the determinant for homogeneous ice nucleation in
676 aqueous solutions, Nature, 406, 611-614, 2000.

677 Lacis, A.: Climate forcing, climate sensitivity, and climate response: A radiative modeling perspective on atmospheric
678 aerosols, Aerosol forcing of climate, 11-42, 1995.

679 Liu, Huang, J., Shi, G., Takamura, T., Khatri, P., Bi, J., Shi, J., Wang, T., Wang, X., and Zhang, B.: Aerosol optical
680 properties and radiative effect determined from sky-radiometer over Loess Plateau of Northwest China, Atmospheric
681 Chemistry and Physics, 11, 11455-11463, 2011a.

682 Liu, Zheng, Y., Li, Z., Flynn, C., Welton, E. J., and Cribb, M.: Transport, vertical structure and radiative properties of
683 dust events in southeast China determined from ground and space sensors, Atmospheric environment, 45, 6469-6480,
684 2011b.

685 Lohmann, U., and Diehl, K.: Sensitivity studies of the importance of dust ice nuclei for the indirect aerosol effect on
686 stratiform mixed-phase clouds, Journal of the Atmospheric Sciences, 63, 968-982, 2006.

687 Mallet, M., Tulet, P., Serça, D., Solmon, F., Dubovik, O., Pelon, J., Pont, V., and Thouron, O.: Impact of dust aerosols
688 on the radiative budget, surface heat fluxes, heating rate profiles and convective activity over West Africa during
689 March 2006, Atmospheric Chemistry and Physics, 9, 7143-7160, 2009.

690 Martonchik, J., Diner, D., Kahn, R., Gaitley, B., and Holben, B.: Comparison of MISR and AERONET aerosol optical
691 depths over desert sites, Geophysical Research Letters, 31, 2004.

692 Miller, R., Tegen, I., and Perlwitz, J.: Surface radiative forcing by soil dust aerosols and the hydrologic cycle, Journal
693 of Geophysical Research: Atmospheres, 109, 2004.

694 Mlawer, E. J., Taubman, S. J., Brown, P. D., Iacono, M. J., and Clough, S. A.: Radiative transfer for inhomogeneous
695 atmospheres: RRTM, a validated correlated-k model for the longwave, Journal of Geophysical Research: Atmospheres,
696 102, 16663-16682, 1997.

697 Nabat, P., Somot, S., Mallet, M., Michou, M., Sevault, F., Driouech, F., Meloni, D., Di Sarra, A., Di Biagio, C., and
698 Formenti, P.: Dust aerosol radiative effects during summer 2012 simulated with a coupled regional aerosol–
699 atmosphere–ocean model over the Mediterranean, Atmospheric Chemistry and Physics, 15, 3303-3326, 2015a.

700 Nabat, P., Somot, S., Mallet, M., Sevault, F., Chiacchio, M., and Wild, M.: Direct and semi-direct aerosol radiative
701 effect on the Mediterranean climate variability using a coupled regional climate system model, Climate dynamics, 44,
702 1127-1155, 2015b.

703 Perlwitz, J., and Miller, R. L.: Cloud cover increase with increasing aerosol absorptivity: A counterexample to the
704 conventional semidirect aerosol effect, Journal of Geophysical Research: Atmospheres, 115, 2010.

705   Phillips, V. T., DeMott, P. J., and Andronache, C.: An empirical parameterization of heterogeneous ice nucleation for
706   multiple chemical species of aerosol, Journal of the atmospheric sciences, 65, 2757-2783, 2008.
707   Seigel, R., Van Den Heever, S., and Saleeby, S.: Mineral dust indirect effects and cloud radiative feedbacks of a
708   simulated idealized nocturnal squall line, Atmospheric Chemistry and Physics, 13, 4467-4485, 2013.
709   Shao: A model for mineral dust emission, Journal of Geophysical Research: Atmospheres, 106, 20239-20254, 2001.
710   Shao: Simplification of a dust emission scheme and comparison with data, Journal of Geophysical Research:
711   Atmospheres, 109, 2004.
712   Shao, Ishizuka, M., Mikami, M., and Leys, J.: Parameterization of size-resolved dust emission and validation with
713   measurements, Journal of Geophysical Research: Atmospheres, 116, 2011.
714   Soil Survey Staff: Soil survey manual, 1993.
715   Solomos, S., Kallos, G., Kushta, J., Astitha, M., Tremback, C., Nenes, A., and Levin, Z.: An integrated modeling
716   study on the effects of mineral dust and sea salt particles on clouds and precipitation, Atmospheric Chemistry and
717   Physics, 11, 873-892, 2011.
718   Su, L., and Fung, J. C.: Sensitivities of WRF-Chem to dust emission schemes and land surface properties in simulating
719   dust cycles during springtime over East Asia, Journal of Geophysical Research: Atmospheres, 120, 2015.
720   Tesfaye, M., Tsidu, G. M., Botai, J., and Sivakumar, V.: Mineral dust aerosol distributions, its direct and semi-direct
721   effects over South Africa based on regional climate model simulation, Journal of Arid Environments, 114, 22-40,
722   2015.
723   Textor, C., Schulz, M., Guibert, S., Kinne, S., Balkanski, Y., Bauer, S., Berntsen, T., Berglen, T., Boucher, O., and
724   Chin, M.: Analysis and quantification of the diversities of aerosol life cycles within AeroCom, Atmospheric Chemistry
725   and Physics, 6, 1777-1813, 2006.
726   Thompson, G., Rasmussen, R. M., and Manning, K.: Explicit forecasts of winter precipitation using an improved bulk
727   microphysics scheme. Part I: Description and sensitivity analysis, Monthly Weather Review, 132, 519-542, 2004.
728   Thompson, G., and Eidhammer, T.: A study of aerosol impacts on clouds and precipitation development in a large
729   winter cyclone, Journal of the Atmospheric Sciences, 71, 3636-3658, 2014.
730   Tomasi, C., Fuzzi, S., and Kokhanovsky, A.: Atmospheric Aerosols: Life Cycles and Effects on Air Quality and
731   Climate, John Wiley & Sons, 2017.
732   Twohy, C. H., Kreidenweis, S. M., Eidhammer, T., Browell, E. V., Heymsfield, A. J., Bansemer, A. R., Anderson, B.
733   E., Chen, G., Ismail, S., and DeMott, P. J.: Saharan dust particles nucleate droplets in eastern Atlantic clouds,
734   Geophysical Research Letters, 36, 2009.
735   Vaughan, M. A., Young, S. A., Winker, D. M., Powell, K. A., Omar, A. H., Liu, Z., Hu, Y., and Hostetler, C. A.: Fully
736   automated analysis of space-based lidar data: An overview of the CALIPSO retrieval algorithms and data products,
737   Remote Sensing, 2004, 16-30.
738   Wesely, M.: Parameterization of surface resistances to gaseous dry deposition in regional-scale numerical models,
739   Atmospheric Environment (1967), 23, 1293-1304, 1989.

740   Winker, Pelon, J., Coakley Jr, J., Ackerman, S., Charlson, R., Colarco, P., Flamant, P., Fu, Q., Hoff, R., and Kittaka,

741   C.: The CALIPSO mission: A global 3D view of aerosols and clouds, Bulletin of the American Meteorological Society,

742   91, 1211-1229, 2010.

743   Winker, D. M., Vaughan, M. A., Omar, A., Hu, Y., Powell, K. A., Liu, Z., Hunt, W. H., and Young, S. A.: Overview

744   of the CALIPSO mission and CALIOP data processing algorithms, Journal of Atmospheric and Oceanic Technology,

745   26, 2310-2323, 2009.

746   Zhang, C., Wang, M., Morrison, H., Somerville, R. C., Zhang, K., Liu, X., and Li, J. L. F.: Investigating ice nucleation

747   in cirrus clouds with an aerosol-enabled Multiscale Modeling Framework, Journal of Advances in Modeling Earth

748   Systems, 6, 998-1015, 2014.

749

750

30

776   Figure 11: Vertical profiles for the mean observed IWC from CALIPSO, and the simulated IWC with various c_f for

777   the dust events on March 21, April 1, April 9, and April 23, 2012.

778   Figure 12: Vertical profiles for the mean observational IWC from CALIPSO, and the simulated IWC with threshold

779   RH values of 105% and 100% for the dust events on March 21, April 1, April 9, and April 23, 2012.

Table 1: Performance statistics for the model in simulating surface PM_{10} concentrations at environmental monitoring stations during the simulation period.

City	STATION NO.	MB (µg/m3)	ME (µg/m3)	RMSE (µg/m3)	r
BAOTOU	XCNAQ77	-36.18	80.43	94.88	0.59
	XCNAQ79	-10.05	75.83	106.58	0.62
SHIZUISHAN	XCNAQ346	72.46	121.18	317.73	0.79
	XCNAQ347	17.64	147.95	294.71	0.75
JINCHANG	XCNAQ340	-108.73	109.09	128.56	0.77
	XCNAQ342	-18.65	46.07	64.78	0.70
YAN'AN	XCNAQ335	-38.93	99.05	149.44	0.68
	XCNAQ336	-60.15	124.74	166.89	0.60
YINCHUAN	XCNAQ344	33.97	112.26	240.27	0.87
	CN_1487	-39.62	155.83	249.00	0.62
Average		-18.84	107.24	181.28	0.70

MB: mean bias; ME: mean error; RMSE: root mean squared error; r: correlation coefficient.
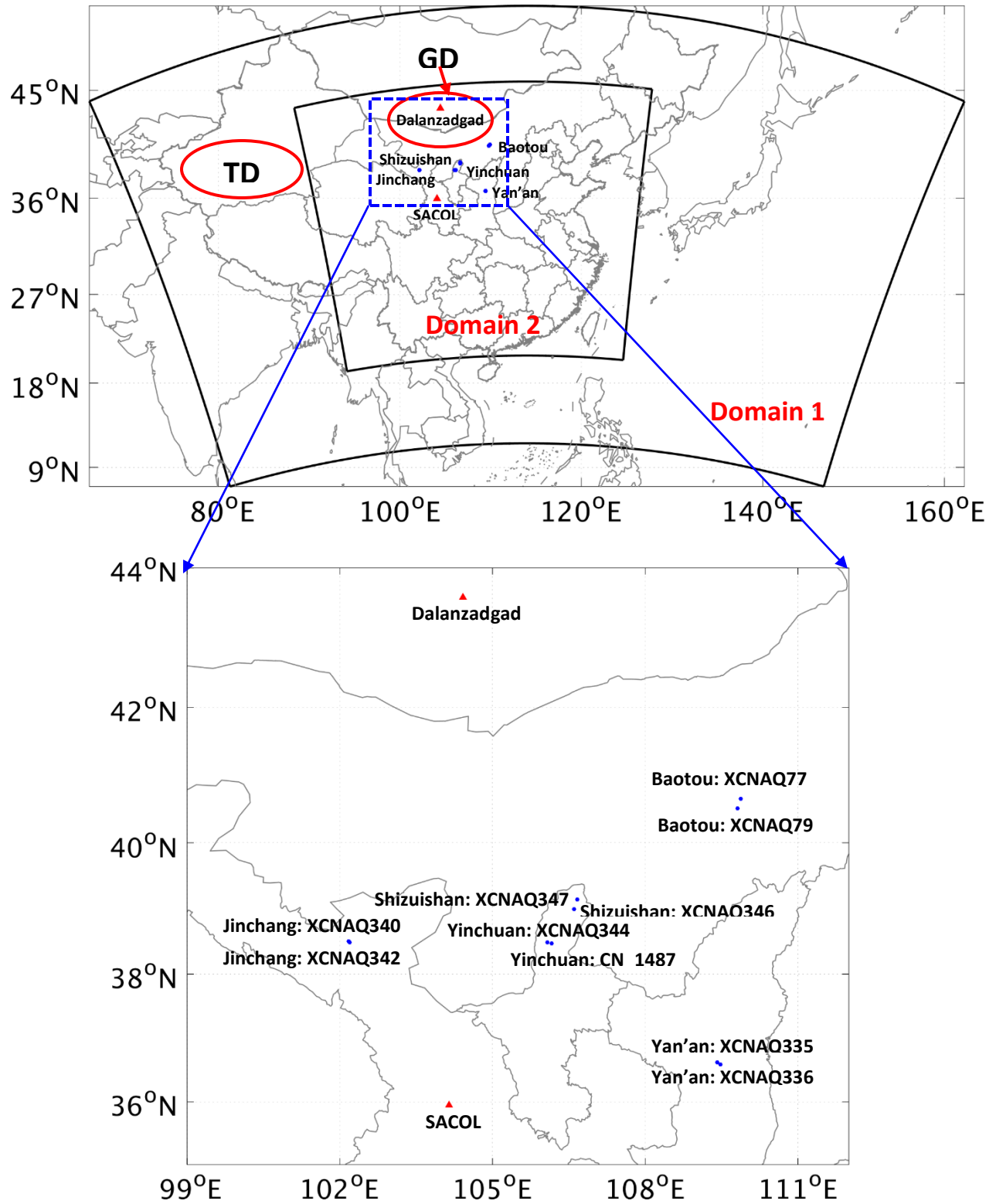
Figure 1: Nested domain set for the simulations. Blue dots represent the ten monitoring stations used for model validation. TD: the Taklimakan Desert; GD: The Gobi Desert.
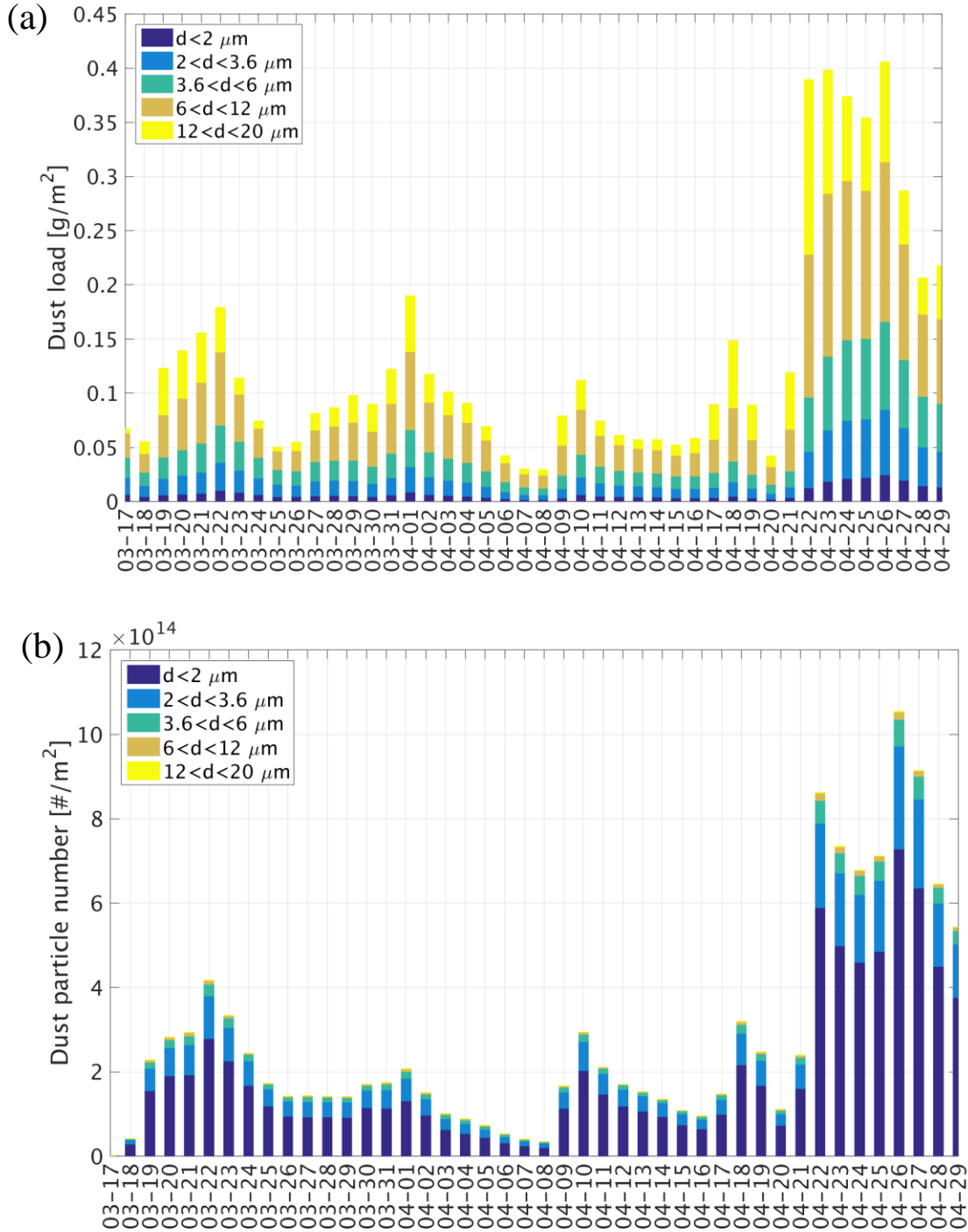
Figure 2: Time series of spatially averaged daily dust mass load (a) and daily number density of dust particles (b) over East Asia (domain 1) during the simulation period.
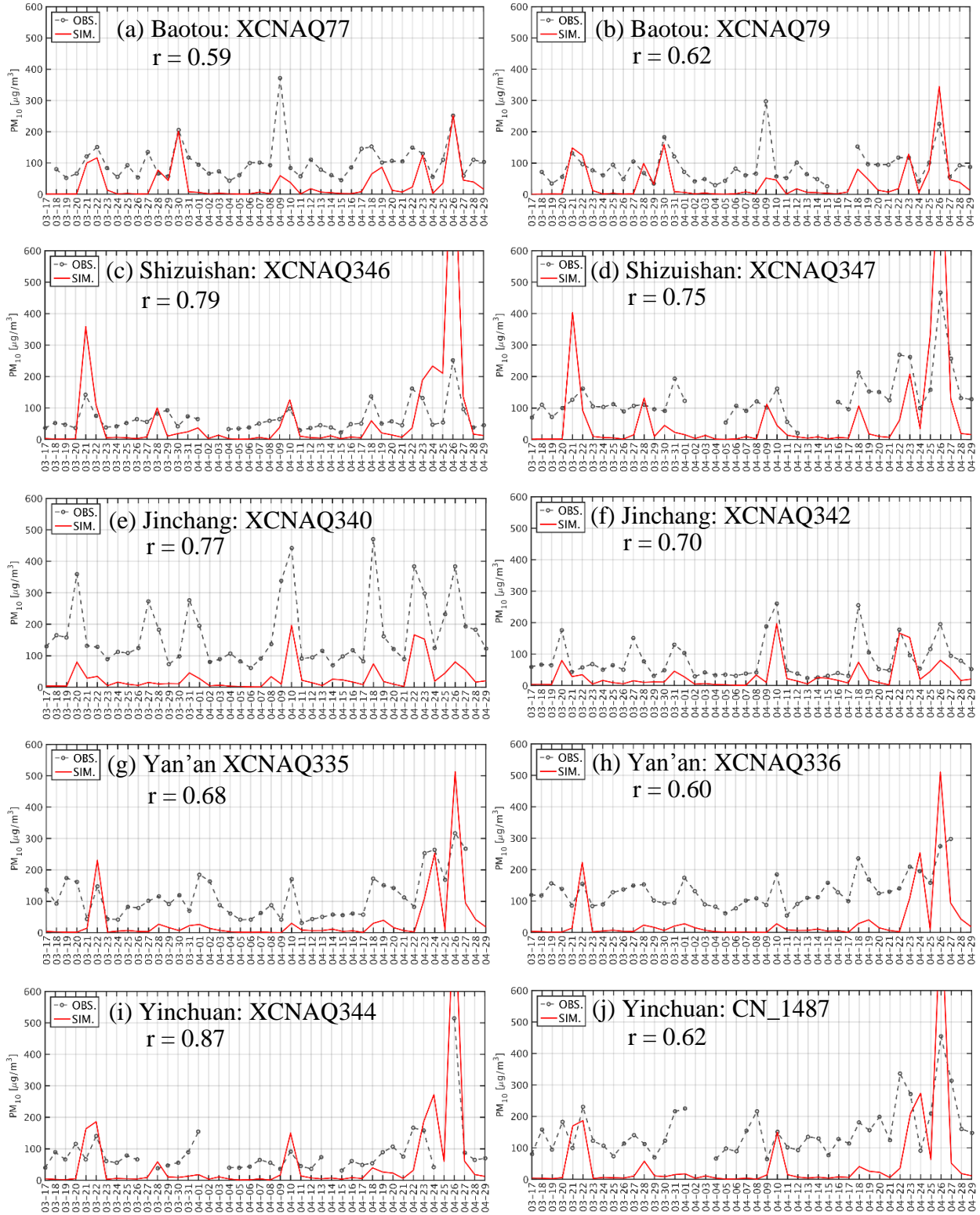
Figure 3: Time series of hourly observed and simulated surface PM$_{10}$ concentrations at various environmental monitoring stations. r represents the correlation coefficient between simulation results and observations.
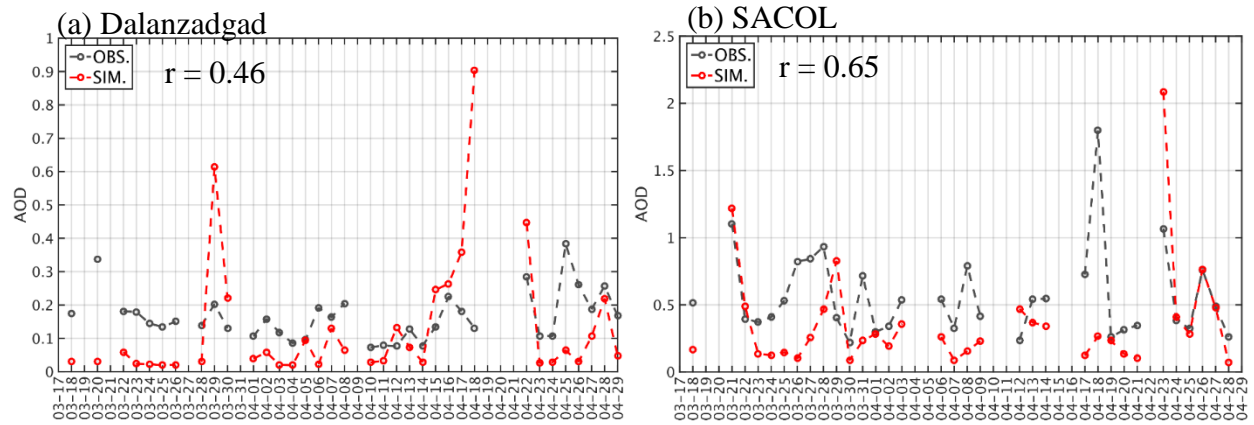
Figure 4: Time series of daily mean observed and simulated aerosol optical depths at Dalanzadgad (a) and SACOL (b). r represents the correlation coefficient between simulation results and observations.
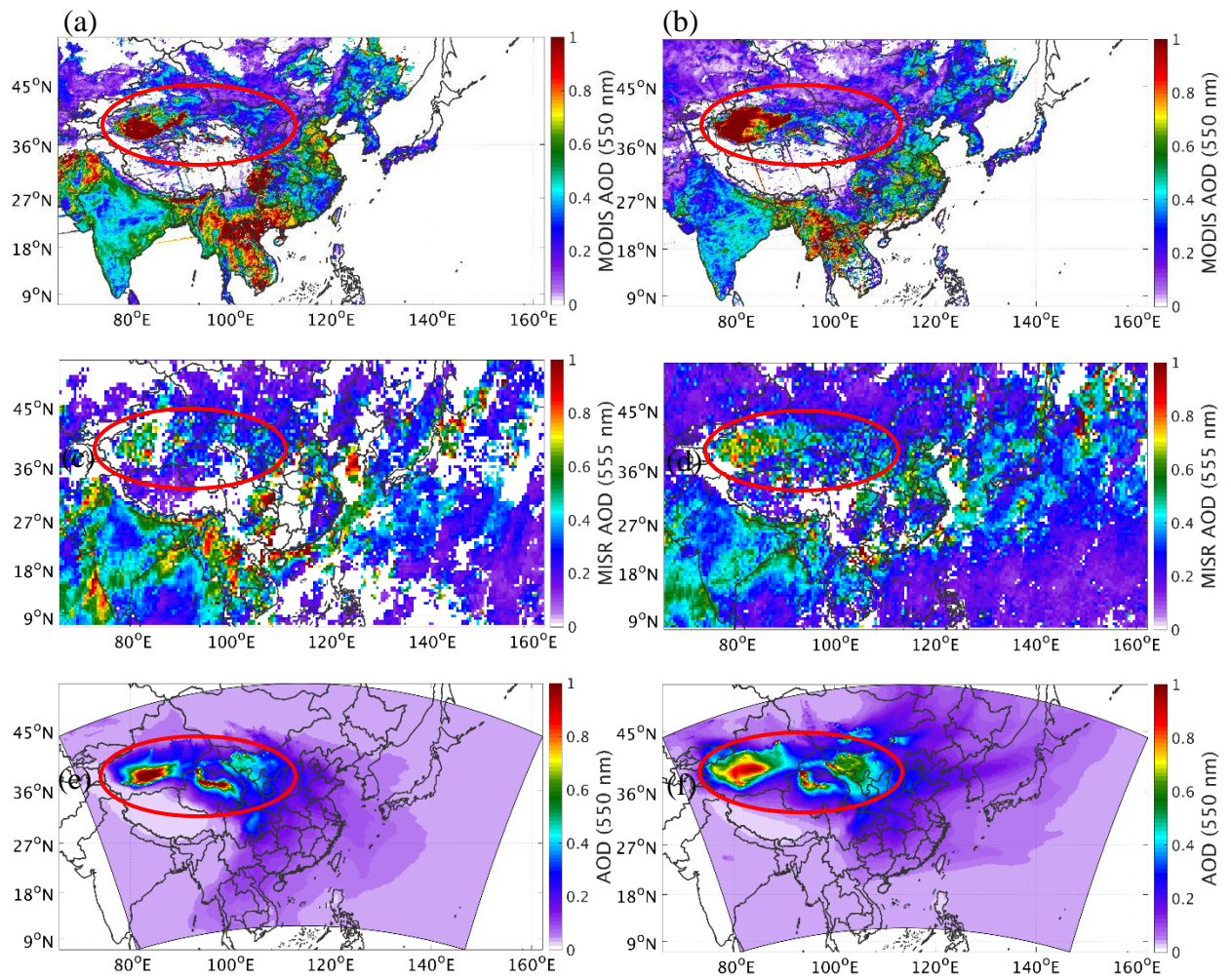
Figure 5: Spatial distributions of monthly mean AOD from MODIS observations (a, b), MISR observations (c, d), and simulation results (e, f) for March (left panel) and April (right panel) of 2012.
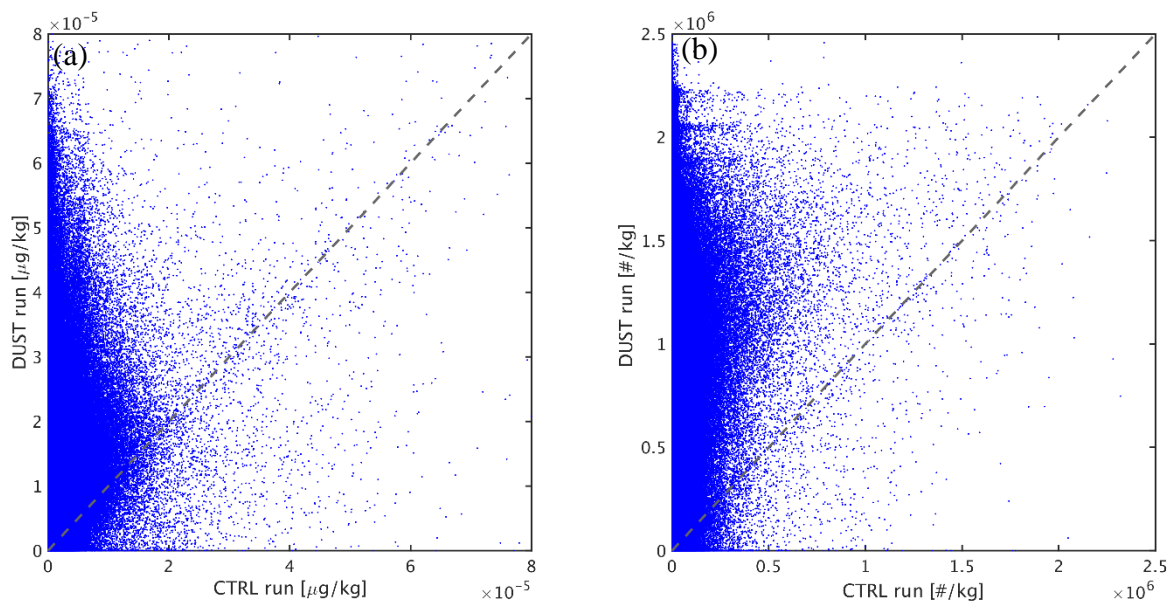
Figure 6: Simulated cloud ice mixing ratio (a) and cloud ice crystal number concentration (b) at each data point from CTRL and DUST.
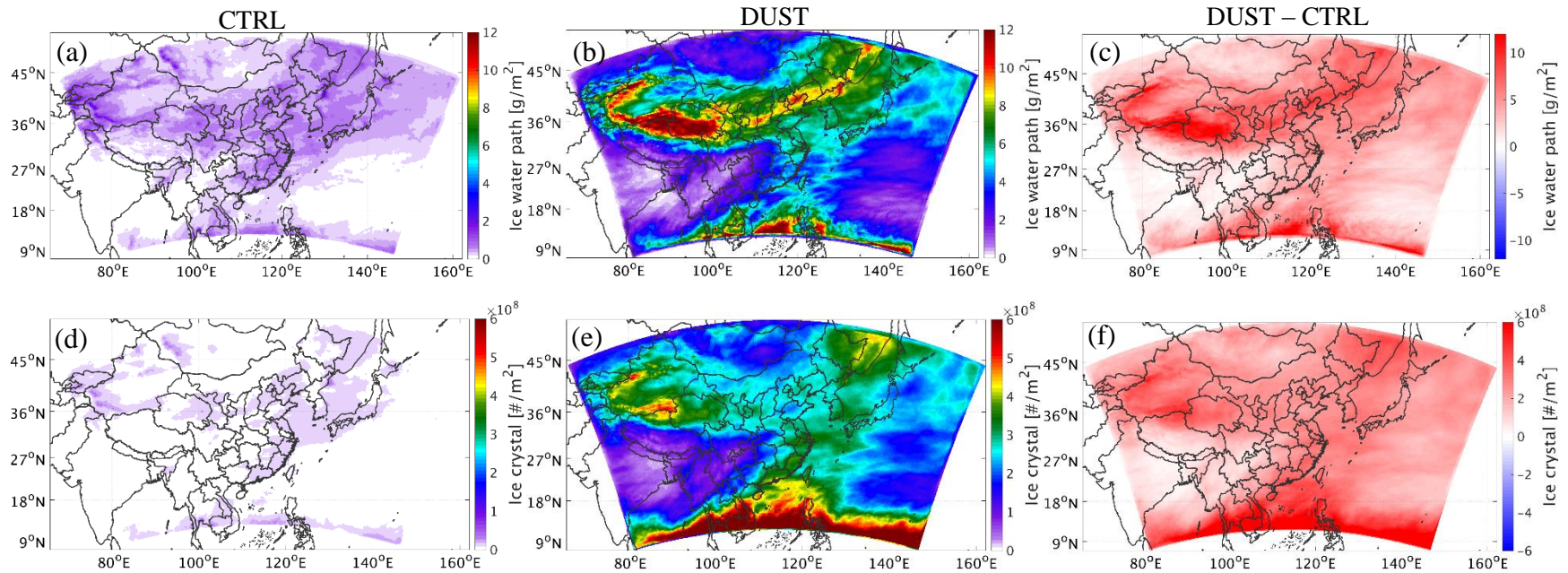
Figure 7: Spatial distributions for the temporal mean simulated cloud ice water path (a-c) and ice crystal number density (d-f) from CTRL (left panel), DUST (middle panel), and the difference between CTRL and DUST (right panel) over East Asia (domain 1) during the simulation period.
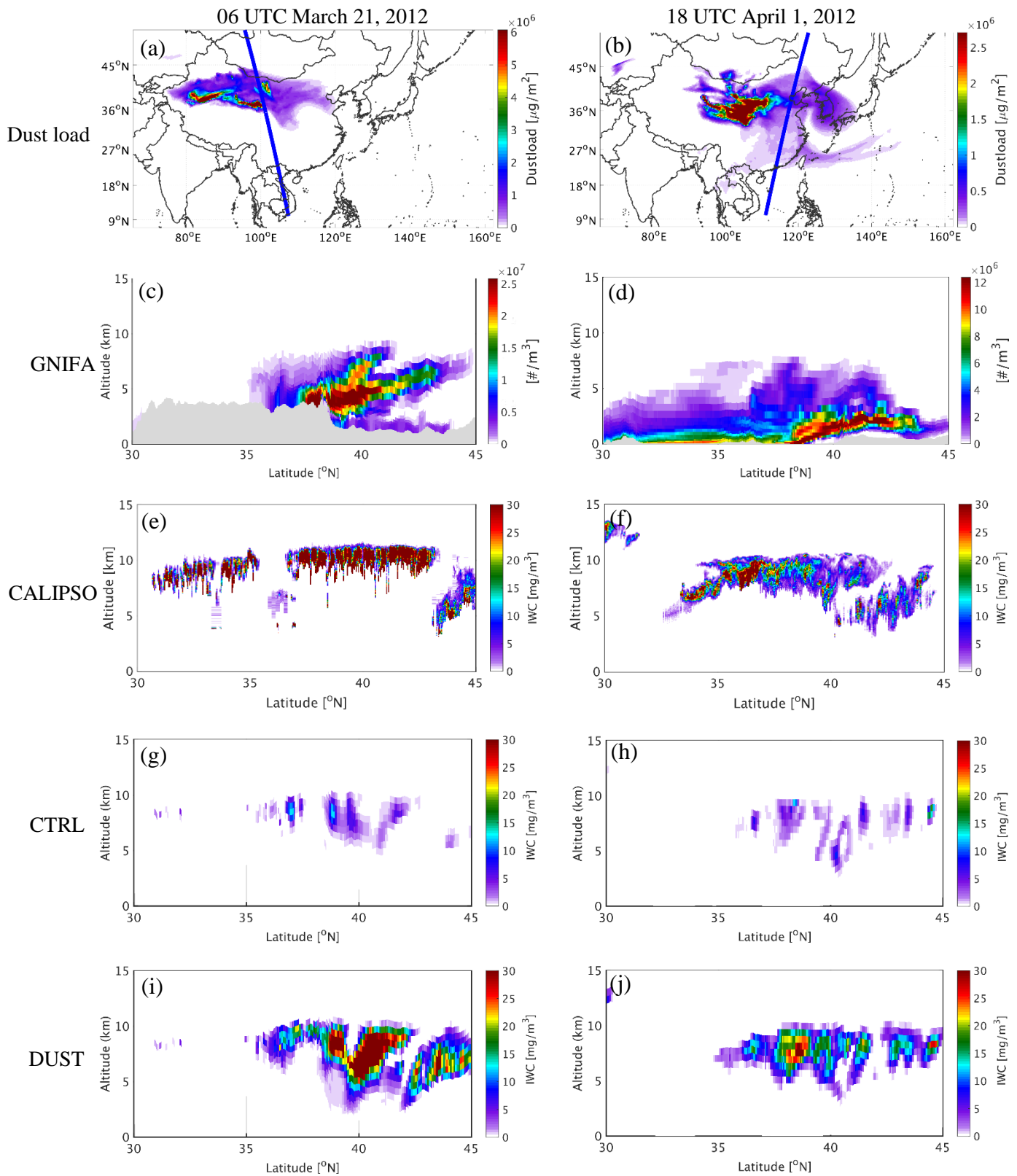
Figure 8: Spatial distribution for simulated dust load and satellite scanning track (a, b); the simulated vertical profile of ice-friendly aerosol (GNIFA) number concentration (c, d), with the orography represented by the shaded area; the CALIPSO vertical profile of IWC (e, f); and the simulated vertical profile of IWC from CTRL (g, h) and DUST (i, j) for the case on March 21 (left panel) and April 1 (right panel) of 2012.
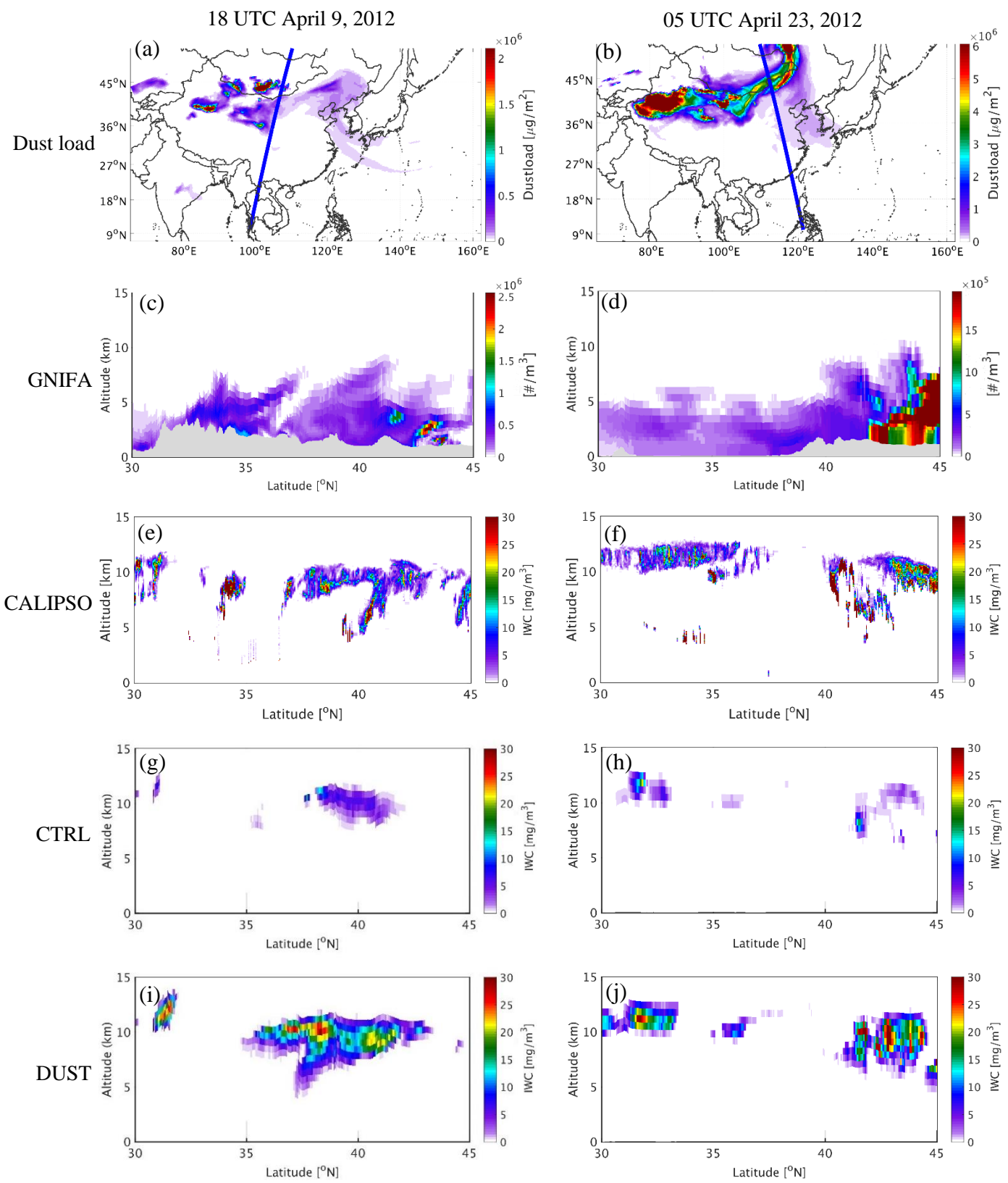
Figure 9: As Figure 8 but for the cases on April 9 (left panel) and April 23, (right panel) of 2012.
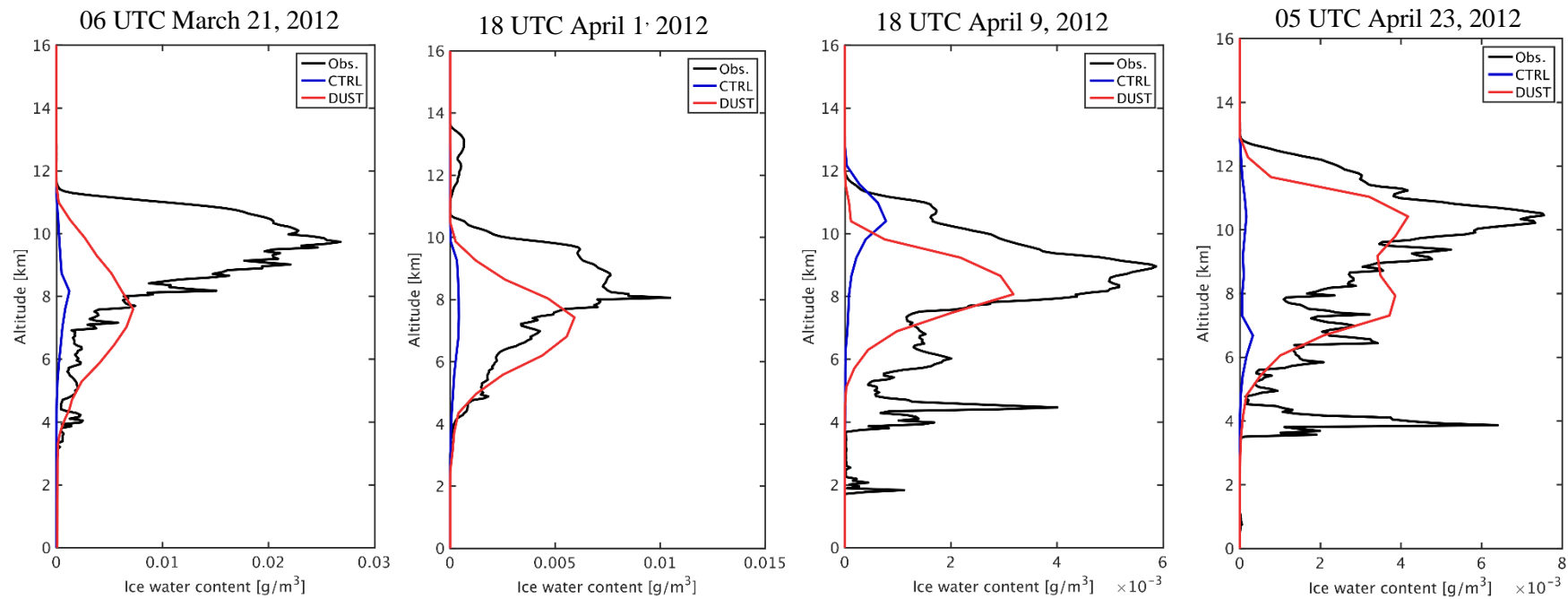
Figure 10: Vertical profiles for the mean observed IWC from CALIPSO, and the simulated IWC from CTRL and DUST for dust events on March 21, April 1, April 9, and April 23, 2012.
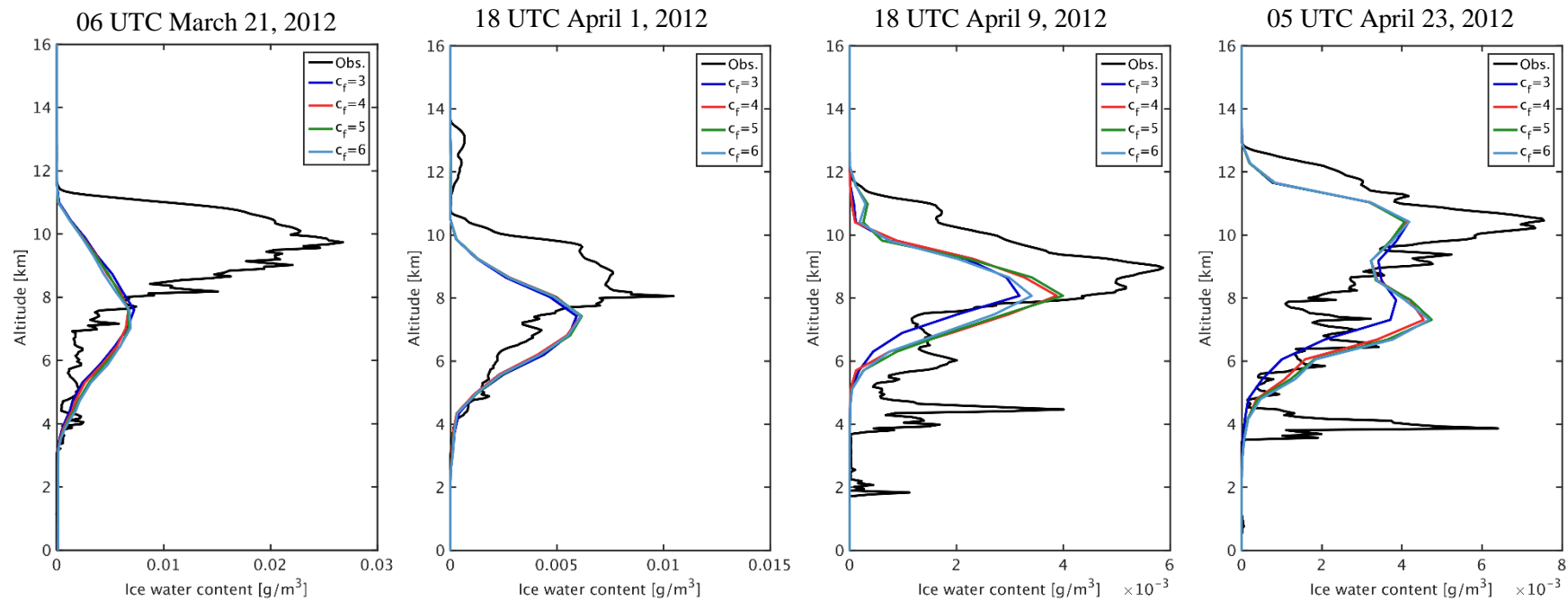
Figure 11: Vertical profiles for the mean observed IWC from CALIPSO, and the simulated IWC with various c_f for the dust events on March 21, April 1, April 9, and April 23, 2012.
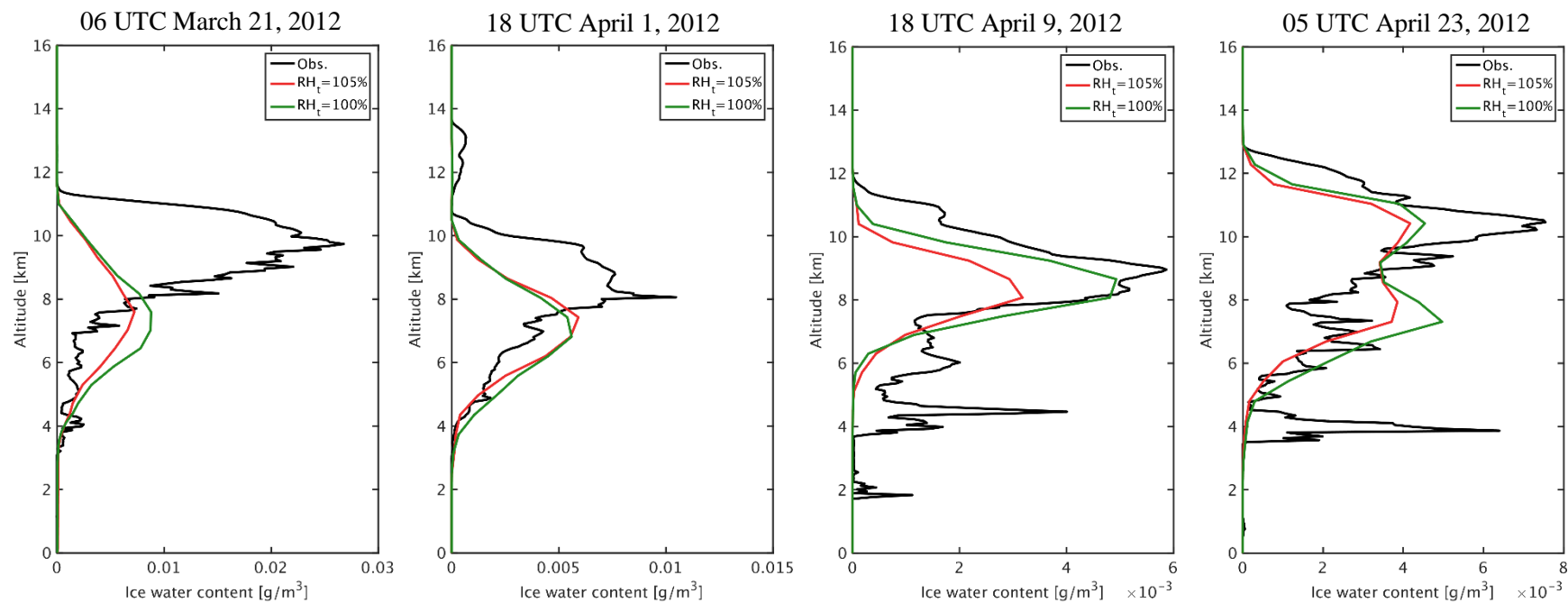
Figure 12: Vertical profiles for the mean observational IWC from CALIPSO, and the simulated IWC with threshold RH values of 105% and 100% for the dust events on March 21, April 1, April 9, and April 23, 2012.